1   # Thermal, compositional, and compressional demagnetization of cementite

2   David Walker[1], Jie Li[2], Bora Kalkan[3, 4] and Simon M. Clark[5, 6]

3   [1]Earth and Environmental Science, LDEO, Columbia University, Palisades, NY 10964, USA

4   [2]Earth and Environmental Sciences, University of Michigan, Ann Arbor, MI 48109, USA

5   [3]Advanced Light Source, Lawrence Berkeley National Laboratory, Berkeley, CA 94720, USA

6   [4]Department of Physics Engineering, Hacettepe University, 06800 Beytepe, Ankara, TURKEY

7   [5]Department of Earth and Planetary Sciences, Macquarie University, North Ryde, NSW 2109 and

8   [6]The Bragg Institute, Australian Nuclear Science and Technology Organisation, Locked Bag 2001,

9   Kirrawee DC, NSW 2232，AUSTRALIA

10

11   # Abstract

12   The 1 bar Curie temperature, T_C, at which cementite (anthropogenic form of the mineral

13   cohenite, nominally Fe_3C) abruptly loses ferromagnetism, is found to be sensitive to small

14   deviations from the stoichiometric cementite composition. Stoichiometric Fe_3C begins to lose

15   magnetic susceptibility at 187 °C. The T_C of ferromagnetic loss in cementite falls by about 13-14

16   °C, in either compositional direction, to the limits at either Fe-saturation or graphite-saturation.

17   Formation of C vacancies in, or C stuffings into, Fe_3C produces non-stoichiometry, disrupts and

18   weakens the Fe magnetic ordering, and produces excess configurational entropy that is

19   proportional to the disruption magnitude. C-excess (~0.6 at.% C) at graphite-saturation is less

20   than the C-deficiency at Fe-saturation (~2.6 at.% C), so the rate at which Curie T_C drops with

21   cementite C% variation is asymmetric about the stoichiometric composition, being steeper on the

22   C-excess side. This asymmetry reflects the higher excess configurational entropy (and

23   consequently greater weakening of Fe magnetic ordering) generated by C excesses than by C

24   vacancies.

25   The application of ~6 GPa pressure to stoichiometric Fe_3C leads to a drop in T_C, of more

26   than 160 °C, to below room T. This large drop in T_C with pressure is shown by loss of

27   ferromagnetism in a specimen compressed in a multianvil device at room T. Densely sampled

28   synchrotron XRD cell volumes through the transition pressure interval at room T show that there

29   is also a small drop in compressibility near 6 GPa for non-stoichiometric cementites. C-rich

30   cementite retains its magnetism to ~1 GPa higher P than C-poor cementite. The drop in T_C with

31   pressure for stoichiometric cementite was tracked in an externally heated diamond anvil cell by

32   the jump in thermal expansion experienced when cementite loses its magnetostriction above T_C

33   (Wood et al., 2004). T_C drops parabolically with pressure, as do the Invar alloys (Leger et al.

34   1972; Winterrose et al. 2009). Both high T and P favor the magnetically disordered (Curie)

35   paramagnetic over the ferromagnetic form of cementite. The observed large positive change in

36   thermal expansion and small negative change in compressibility at the T_C transition give a good

37   quantitative account of the negative dT_C/dP slope mapped by the ferro-paramagnetic phase

38   stability boundary through Ehrenfest's (1933) second relation.

39   Our observations of cementite demagnetization at P~6 GPa, room T confirm the

40   synchrotron Mössbauer work of Gao et al. (2008). The demagnetization pressures based upon

41   experiment are lower than those estimated from existing theoretical treatments by ~ an order of

42   magnitude. Stability calculations for carbide in the mantle and core are influenced by the choice

43   among ferromagnetic, paramagnetic, and non-magnetic equations of state. Because the

44   ferromagnetic phase is more compressible, the calculated P-T range for cementite stability would

45 be too large under the assumption of ferromagnetism persisting to higher pressures than shown

46 here experimentally. Our results diminish the theoretical P-T range of cementite stability.

47 Key words: cementite, magnetism, Curie temperature, composition, pressure, stability.

1. Introduction

49   There has been a recent resurgence of interest in the carbide minerals (Wood, 1993; Scott

50 et al., 2001; Li et al., 2002; Vocadlo et al. 2002; Lin et al., 2004; Gao et al., 2008, 2011; Lord et

51 al., 2009; Dasgupta et al., 2009; Nakajima et al. 2009, 2011; Dasgupta and Hirschmann, 2010;

52 Ono and Mibe, 2010; Mookherjee et al. 2011; Mookherjee, 2011; Buono, 2011; Buono et al.,

53 2013: Dasgupta, 2013; Walker et al., 2013; Chen et al., 2012, 2014) such as cementite as mantle

54 and core constituents in the Earth. Assessing the potential for these minerals to be stable at depth

55 requires extrapolation of density to mantle and core pressures. Any changes in the magnetic state

56 of the material will affect this extrapolation and so needs to be well documented. Existing studies

57 show large discrepancies in the pressure of demagnetization in cementite, ranging from 6 to 22

58 GPa in experimental results (Lin et al. 2004, Duman et al. 2005, Gao et al. 2008, Prescher et al.

59 2014) to 55 to 60 GPa from theoretical calculations (Vocadlo et al. 2002, Ono and Mibe 2010,

60 Mookherjee et al. 2011). The recent demonstration of non-stoichiometric forms of cementite

61 (Walker et al., 2013; confirming and extending Petch, 1944) suggests a possible explanation of

62 some of these discrepancies. The previous studies of cementite used indirect methods of

63 determining the loss of magnetization with pressure. Here we present a direct measurement of

64 loss of magnetization with pressure by monitoring magnetic susceptibility of stoichiometric

65 cementite inside a multi-anvil press up to 7.5 GPa.

66   Monitoring kinks in the rate of change of volume has been shown to be a feasible method

67 for determining loss of magnetization with changing temperature for cementite by (Wood et al.

68 2004) and with changing pressure for Fe_7C_3 (Nakamajima et al., 2011; Chen et al. 2012) and also

69 for the Fe-Ni and Fe-Pt Invar alloys (Oomi and Mori, 1981a,b)). Volumetric kinks, however,

70 have not been previously reported for cementite in the pressure regime of our studies (Scott et

71 al., 2001; Li et al., 2002; Duman et al. 2004; Prescher et al., 2012). Duman et al. (2004) did

72 show that compressibility of 40 nm particles of Fe_3C above T_C was smaller than at room T

73 without sufficient pressure sampling to determine whether the transition was sharp at T_C. This

74 leads us to ask whether the lack of kinks in the non-nano studies is due to poor sampling across

75 potential transitions. Here we present the results of studying the demagnetization of non-

76 stoichiometric cementite as a function of temperature and pressure using the indirect method that

77 associates volumetric kinks with magnetic phase transitions. We measured the high-resolution

78 isothermal compression curves of carbon-saturated and iron-saturated compositions at room

79 temperature, using synchrotron X-ray-irradiated diamond anvil cell (DAC) with fluid pressure

80 medium. We also used the jump in thermal expansion, following Wood et al. (2004), in an

81 externally heated DAC to monitor the demagnetization T_C of stoichiometric cementite with

82 pressure.

83   Together these approaches allow us to map out the demagnetization of cementite as a

84 function of temperature, pressure, and stoichiometry and to examine the nature of the

85 demagnetization transition by comparing changes of thermal expansion and compressibility of

86 cementite at the magnetic transition with dT_C/dP as described by Ehrenfest's second relation.

87 Finally, we discuss allowable choices for the equation of state for cementite and the expected

88 instability of cementite at mantle and core pressures.

2. Experimental procedure

89

2.1 Cementite synthesis

90

91   Fully dense, ~200 mg, polycrystalline, cylindrical cementite (±Fe±graphite) ingots were

92   grown from mixed starting powders of Fe metal and graphite at 1 GPa, 1110 °C in a ½" piston

93   cylinder device following procedures in Walker et al. (2013). Four samples were studied: one

94   stoichiometric sample, one saturated with carbon, one over doped with iron, and one saturated

95   with iron. Table 1 gives the charge compositions, phase assemblages, and annealing times for the

96   samples used in the present study (synthesized during our earlier study where details of phase

97   synthesis and microprobe analytical protocols are given). The long anneal times with minimal

98   subsequent physical disruption was intended to minimize mechanical strains that might have an

99   effect on Curie T_C magnetic properties. A typical half ingot is shown in figures 1a and 1b before

100   and after the high pressure magnetic measurements. For all magnetic measurements, the

101   integrity of the ingots after the long 3-5 day anneal, thermal quenching, and rapid

102   depressurization was compromised only by splitting with a chisel into 2-3 chunks of 3-5 mm

103   dimensions.

104   **Fig 1**

2.2 Magnetic susceptibility detection at ambient pressure

105

106   Our objective was to observe changes in magnetic susceptibility in cementite at

107   multianvil pressures. Preliminary development at ambient P of suitable sensor mechanisms and

108   circuits that could eventually be incorporated within a multi-anvil assembly was undertaken to

109   optimize sample size, position, sensor activation, and detection circuits.

110   Figure 1c illustrates the experimental configuration used to investigate the effect of

111   compositional variation in cementite upon T_C. The approach taken was to wind a coaxial pair of

112   induction coils, each from about 2 feet of 0.008" enameled Cu wire, around a flanged cylindrical

113   Cu form of about ¼" inner diameter into which the sample was placed. When the cementite is

114   ferromagnetic, it behaves as the magnetic core to a transformer so that an alternating current in

115   the primary winding produces an alternating current in the secondary winding. This

116   "transformer" strategy resembles that of Leger et al. (1972). We dispensed with the toroidal core

117   of Leger et al. (1972) for experimental convenience, because it is more difficult to fabricate a

118   dense, annealed toroid of cementite than our arbitrary ingots. We ensure adequate inductive

119   coupling is achieved between our coaxial windings through high winding density. The inductive

120   transfer was detected through an AC microvoltage on the secondary coil. To test this system we

121   first attempted to measure the known Curie temperature at ambient pressure. The coaxial, coiled

122   sensor with its enclosed ingot (Figure 1c) was heated within a small non-inductively-wound

123   electric resistance furnace while the secondary coil and thermocouple microvoltages were

124   monitored. A 15V primary AC voltage was initially tuned using a variable resistor to give

125   between 100-200 microvolts on the secondary coil with a magnetic test piece (Figure 1c). This

126   signal indicates the presence of magnetism and the loss of the signal indicates the loss of the

127   magnetism.

128   **2.3 Multianvil adaptations to monitor susceptibility at high pressure**

129   Our preliminary ambient pressure experimental configuration was sized to be compatible

130   with eventual insertion within a multianvil apparatus using octahedral pressure media

131   compressed by corner-truncated tungsten carbide cubes with 12 mm facets within a

132   cube/octahedral anvil arrangement (Walker et al. 1990). Once the basic feasibility of T_C

133   detection using these circuits for this size sample was demonstrated, moving from temperature to

134   pressure measurements required some modifications to the original design (Fig. 1d). These

135   included elimination of the non-inductive heater, which always failed during preliminary

136   compression. The Cu winding form was replaced with machinable MgO to avoid short circuiting

137   the induction coils. The 2 windings, of ~equal numbers of turns, were formed from 3' of 0.008"

138   enameled Cu wire. The space between the cementite ingot and the inside of the MgO form was

139   firmly packed with KBr as a space-filling pressure-transmitting material that would minimize the

140   internal deformation and strain of the ingot. Electrical connections to the coils were effected

141   through 4 of the tungsten carbide (WC) cubes by running the 4 coil leads to each of 4 separate

142   truncated triangular cube faces (Fig. 1e). The entire assembly of coils and MgO form was

143   vacuum impregnated with epoxy to stabilize the coils from internally short circuiting during

144   compression.

145   **2.4   Pressure calibration for nonstandard multianvil techniques**

146   Multiple compression cycles with iteratively improved coil contacts were attempted

147   before stable electrical signals were obtained (Figure 1e). Through each successive compression

148   it was necessary to substitute/add pyrophyllite gasket fins of 2x3 mm cross section to the normal

149   castable ceramic 584OF gaskets integral to the pressure medium octahedron in routine use in the

150   Lamont-Doherty Earth Observatory (LDEO) laboratory. The gaskets (and some extruded

151   pressure medium) disintegrate upon decompression and are not reusable even though the

152   remainder of the octahedron, ingot, and internal coils are. Our standard calibrations are only

153   valid for a single compression cycle. Furthermore, as none of our previous 12 mm truncated edge

154   length (TEL) assemblies have been vacuum impregnated with epoxy, nor vexed through 4

155   compressive cycles, we performed calibrations of such an assembly sent through an analogous 4

156   cycles of re-gasketing and compression with Bi in a 4-wire resistance circuit as the calibrant.

157   We carried out our calibrations over multiple compression cycles in exactly the same manner as

158   we collected the susceptibility data in order to be sure of our pressures in the final cycle.

159   **2.5 Electrical resistance measurements of stoichiometric cementite**

160   In order to check for any structural phase transition at the point of demagnetisation we

161   also collected DC conductivity data from a stoichiometric sample of cementite. A 4-wire circuit

162   like that used to observe the electrical changes in Bi resistance during pressure calibrations

163   (Figure 1f) was applied to a 1.5x3 mm cylinder of compacted cementite chips from sample HX-

164   26. Voltage, proportional to the sample resistance, was monitored to 8 GPa at room temperature.

165   **2.6 X-ray diffraction measurements on stoichiometric cementite in an externally heated-**

166   **diamond anvil cell**

167   Thermal expansion of the stoichiometric cementite unit cell was monitored as a function

168   of pressure using synchrotron X-ray diffraction at beamline 12.2.2 of the Advanced Light

169   Source, Lawrence Berkeley National Laboratory (Fig. 2A). This beamline is dedicated to high-

170   pressure studies and has a fully automated sample alignment system. The X-ray energy was

171   chosen to be 25keV and the sample to image plate detector distance set to about 440mm and

172   calibrated using the NIST LaB$_6$ standard. The standard energy calibration procedure at BL12.2.2

173   is to collect absorption data from a reference metal foils with K-edges at around 20-30 keV and

174   to calibrate the wavelength/energy according to the position of the K-edge to agree with its

175   reference value. Typical error is ±1-2 eV. This procedure is done periodically, but not for each

176   user shift. For each user shift and each stage reloading, the energy error, if any, is folded into

177   sample to detector distance error determined from the LaB$_6$ standard. The X-ray beam size was

178   set to 20x20 microns. Exposure times were typically 2-5 minutes. Image plate data was

179   integrated with Fit2D (Hammersley et al., 1996) and peak positions were determined with XFIT

180   software (Cheary and Coehlo, 1996). Indexing and cell refinements were done with CELREFv3

181   software (Laugier and Bochu, 2003). Typically 12-20 peaks were indexed and refined to obtain

182   unit cell parameters. However particular attention is paid to the (200) peaks for reasons

183   explained in section 3.4.

184   Pressures were generated using a diamond anvil cell (DAC) driven by a gas membrane.

185   Gas pressure was controlled remotely by an automated Ar pumping system. Initial and final

186   sample pressures were determined using an off-line ruby fluorescence system. An internal NaCl

187   diffraction standard within the DAC chamber with the cementite and the pressure medium was

188   used to determine the sample pressure at each pressure-temperature point (Birch, 1986). The

189   NaCl was included as a flake, hand-pressed to optical clarity between two WC blocks. The

190   cementite starting powders were also pressed into flakes by this same method. Re sample gaskets

191   of 250 micro meter thickness for use with 150 micron diamond culets were pre-indented by those

192   culets to ~70-100 micro meter thickness and then drilled to form a 75 micro meter inside

193   diameter (ID) cylindrical sample chamber. Methanol : ethanol mixture (4 : 1 by volume) was

194   used as a pressure medium, being mixed from fresh stock within a day of the start of any cycle of

195   beam time measurements. Temperature was raised above room T using an electric resistance

196   band heater in direct contact with the outer diameter of the DAC cylinder. Temperature

197   measurement was performed by a type K thermocouple in direct contact with both the DAC

198   gasket and cylinder diamond. PID feedback control of the temperature was automatically

199   performed through incremental control of the band heater's power supply to ± 1 °C. The band-

200   heater/DAC was thermally isolated from the station 12.2.2 positioning stage by a Cu stand with

201   aggressive internal fluid-cooling. (Figure 2A).

202   **Fig. 2**

203   Our experimental protocol was to load flakes of NaCl internal pressure standard,

204   cementite, and ruby for fluorescence checking, into the DAC, fill the sample chamber with

205   methanol : ethanol pressure medium, and hand tighten until sealed. Fluorescence pressure was

206   checked and the cell mounted on the 12.2.2 end station positioning stage in its heating jacket.

207   Alignment of the cell in the X-ray beam and indexing to the stage's rotation axis followed.

208   Simultaneous diffraction exposure of NaCl and cementite was followed by application of heating

209   to reach a new temperature at the selected pressure, realignment and position indexing, re-

210   exposure to the beam to collect new XRD patterns, etc. At the end of the highest temperature

211   diffraction measurement the cell was cooled back to room temperature and pressure checked to

212   complete the thermal expansion cycle. After each thermal expansion cycle, the pressure was

213   increased by the gas pumping system and a new thermal expansion cycle initiated. The highest

214   pressure cycle overshot to almost 9 GPa after the previous cycle of about 5 GPa. After this cycle

215   the DAC was fully depressurized and a zero-pressure thermal expansion cycle (HX26 run 7) was

216   performed. Figure 2B shows a stack of integrated XRD patterns from the thermal expansion

217   cycle of stoichiometric HX26 run 7.

218   **2.7 X-ray diffraction measurements as a function of pressure for iron or graphite saturated**

219   **samples**

220   Small accessory flakes from the sample splitting were gently crushed to powder for use in

221   diamond anvil cell (DAC) measurements at ambient temperature in the same manner as for the

222   thermal measurements of the previous section. We compressed the two extreme compositions of

223   cementite (Fe-saturated HX-39 and graphite-saturated HX-32) to ~10 GPa, beyond which

224   pressure the methanol : `ethanol pressure medium freezes, introducing the unwanted

225   complication of additional nonhydrostatic stresses; these were avoided, by restricting our

226   pressure range. NaCl foils were again used as pressure calibrants for each XRD pattern. The

227   sample alignment procedures are the same as for the thermal expansion cycles, except the

228   pressure between patterns was changed incrementally, instead of the temperatures.

3. RESULTS and DISCUSSION

230   **3.1 Asymmetric variation of T_C with composition of cementite**

231   Experimental results at room pressure for four cementite compositions (including

232   duplicates on separate pieces of different mass of stoichiometric Fe_3C HX-26) are given in Table

233   1 and Figure 3. In these room pressure magnetic susceptiblity experiments, we observed sharp

234   drops in the secondary coil microvoltages when the cementite lost its magnetic susceptibility

235   with increasing T. We assigned the Curie temperature T_C to the first temperature at which the

236   secondary voltage abruptly begins its steep descent (Fig. 3). Iteration of winding density,

237   activation voltage, wire gauge, coil dimensions, heating rate and other experimental parameters

238   produced large, easily measured, reproducible signals from our annealed cementite ingots. It was

239   possible to recognize and reproduce measurements of T_C to within ±1 °C during both heating and

240   cooling cycles without hysteresis. Duplicate HX-26 measurements on different sample splits

241   were within 1 °C of each other. This experimental reproducibility sets the T error bars in Figure

242   3c.

243   The 187 °C T_C for loss of ferromagnetism in Fe_3C agrees with the abrupt transition to

244   high thermal expansion found by Wood et al. (2004) at 187 °C. The composition of Wood's

245   cementite is not known, but from its synthesis method is likely to be more C-rich than

246   stoichiometric. [The 187 °C that we quote for Wood et al. (2004) comes from their data figures

247   which show the volumetric and lattice parameter transition at 20 °C below the T_C value quoted in

248   their abstract.] The magnetic susceptibility background above T_C is higher for HX39 because of

249   the small α-Fe content in its bulk composition of low C content. The composition of the

250   cementites in HX35 and HX39 are very close to the same as each other (Walker et al. 2013) even

251   though the bulk compositions differ. The larger C-deficiency in the HX39 bulk composition is

252   accommodated by the small proportion of saturating α-Fe in the product ingot. Results are

253   summarized as a function of bulk composition in Figure 3c.

Fig. 3

254   The most stable composition of cementite for magnetic ordering is stoichiometric Fe_3C

255   (Figure 3c). Likewise stoichiometric FePt, FePd, and $FePd_3$ in the literature are most resistant to

256   thermal demagnetization compared to their neighboring non-stoichiometric alloys (Wijn, 1991).

257   Departures from stoichiometry commonly lead to diminished T_C, as if disruption of the

258   arrangement of constituents in off-stoichiometric materials were also destabilizing the magnetic

259   ordering. It takes less thermal energy to disrupt the magnetic ordering in less compositionally-

260   well-organized, off-stoichiometry materials, and so T_C drops with departure from stoichiometry.

261   Qualitatively we expect the observed maximum in T_C at stoichiometric Fe_3C.

262   We now inquire into the striking asymmetry shown by the decrease of T_C with

263   compositional direction in Figure 3c. The drop in T_C with C content is distinctly more rapid

264   towards cementites that are more C-rich than stoichiometric. Why? Excess configurational

265   entropy is a useful measure for the disorder introduced by chemical modification, and it may

266   provide a rough guide to how much destabilization of the related magnetic ordering to expect, at

267   least in a relative sense, in one compositional direction compared to the other. If excess

268   configurational entropy is generated at a higher rate by C excess than by C vacancy, and if C

269   excesses and vacancies are the mechanisms by which cementite departs from stoichiometric

270   Fe_3C, then the sense of asymmetry in our reduction in T_C is explained. T_C should fall faster in the

271   C-rich direction than in the C-deficient direction, as it does. This explanation supposes that the

272   entropy derived from C placements and removals have an effect on their neighboring Fe (the

273   active ingredient in the magnetism), so the magnetic consequences are indirect effects of the

274   constituent entropy generated by the C configurations. Warps and distortions of the C lattice

275   introduce complementary degradations of the Fe arrangement which is most stably ordered in the

276   stoichiometric version.

277   **Fig 4**

278   But why does the formation of C vacancies produce less ideal excess configurational

279   entropy than C excesses? The preferential occupancy of C in the interstitial sites along the pleats

280   in the close-pack Fe layers provides a notional mechanism for this asymmetry. See Figure 4. C

281   deficiency can be distributed as vacancies over these nominally-filled, pleat-related sites with an

282   ideal configurational entropy that is roughly half that of the ideal configurational effect of

283   accommodating excess C by partial filling of the other normally vacant interstitial sites that are

284   not associated with the pleats. This is because there are half as many sites over which to

285   distribute vacancies as there are alternate non-pleated sites over which to distribute excess C.

286   The observed difference in the rates of T_C decrease on either side of stoichiometric Fe_3C is in the

287   correct sense and is roughly this factor of two.

288   Figure 5 summarizes some features of our explanation in terms of the variation of G

289   (Gibbs energy) as a function of C content for cementites at $T>T_C$ and at $T<T_C$. Both

290   ferromagnetic and paramagnetic forms of stoichiometric Fe_3C must be stable at the T_C for

291   stoichiometric cementite, so the kinks in the blue and red curves (corresponding to stoichiometric

292   paramagnetic and ferromagnetic cementite) will touch at T_C. This would occur in between the

293   two temperatures we have shown. At $T<T_C$ there is a field of compositions around the

294   stoichiometric Fe_3C where the (red) ferromagnetic phase is more stable (lower G) than the (blue)

295   paramagnetic. This corresponds to the region under the 'hoop' in Figure 3c. The configuration of

296   the compositional curvatures in $G(X_C)$ dictates that the 'hoop' is asymmetric. Specifically the

297   steeper increase of G with X_C to the C-rich side of Fe_3C for the ferromagnetic phase, requires

298   that the T variation of T_C with X_C is steeper on the C-rich side of Fe_3C. [$T_C(X_C)$ is given by the

299   intersection of the red and blue G curves.] This means that X_C of the T_C branch on the C-poor

300   side is farther from Fe_3C than on the C-rich side at each $T<T_C$. The steeper increase of G on the

301   C-rich side which drives this asymmetry cannot just be a result of the excess configurational

302   entropy invoked above. Such entropy would lower rather than raise G. Rather we must rely on a

303   cooperative coupling to magnetism to cause a rise in G for the magnetic phase over the

304   paramagnetic.

Fig. 5

305   Additional features of note in Figure 5 are the different possible treatments we have

306   accorded the C-rich and C-poor branches of the diagram. The choice was arbitrary for this

307   illustrative purpose. To the C-rich side we supposed that the normally considered situation

308   applies, namely that C is immobile on the time scale of the experiment. Cementite has only a

309   single composition imposed by the bulk composition which is either ferromagnetic or not. Under

310   this partial constraint, *G* minimization dictates a single choice for the composition of both stable

311   coexisting ferro- and paramagnetic cementites - at the vertical dotted line labeled 'constrained

312   equilibrium'. However if we relax the C immobility constraint then the situation shown

313   arbitrarily on the C-poor branch might apply. There *G* minimization dictates C-partitioning

314   between a pair of the ferro- and paramagnetic cementites with the paramagnetic cementite being

315   more C-poor. The equality of *G* constraint is evaded, for these coexisting solutions in which X_C

316   is not the same, by substitution of the requirement that $\bar{G}_{Fe}$ must be the same in each phase, as

317   must $\bar{G}_C$ match in the phases. The notional solution is given by the two vertical dotted lines

318   labeled Fe-C partitioning. We do not expect to encounter this partitioning at T_C in the

319   neighborhood of 200 °C during the age of the Earth for kinetic reasons. However partitioning

320   might be a more experimentally accessible phenomenon in more magnetically robust systems

321   like Fe-Si with Curie T_C nearer 800 °C.

3.2 Reduction of T_C with pressure

323   Our high-pressure susceptibility experiments showed that KBr was remarkably effective

324   at preventing the normal mashing of samples experienced in a multianvil experiment. The ingot

325   of stoichiometric cementite (HX-26) used is only cracked from before to after 4 cycles of

326   pressurization, decompression, regasketing, and finally dissolutive extraction from the assembly,

327   as seen in Figure1b. Never the less we only achieved stable measurements from the assembly on

328   the 4th compression, the coil leads being the weak link in the circuits. The 4th try produced very

329   stable signals. Evidently the coils survived the previous 3 compressions of up to 400 tons without

330   damage. However the use of multiple compressions, decompressions, and regasketings raises

331   issues of what pressure calibration to use as the assembly evolves with continued cycling. This

332   unusual procedure requires some presentation of calibration results and discussion before we

333   inspect the magnetic susceptibility results for which the iterative procedure was needed.

334   **Fig. 6**

335   Figure 6 shows the results of our 4-cycle calibration for the force applied vs. the pressure

336   achieved that we use to interpret our demagnetization results. The 4th cycle is only a little

337   degraded in efficiency at converting thrust into sample pressure compared to the normal

338   calibration that we (and others) use for cold 12 mm TEL experiments (e.g. TT-960), perhaps a

339   somewhat surprising and encouraging result. The pressurization efficiency is unusually large for

340   these 2nd and 3rd compressions because the initial void spaces in the 584OF have been removed

341   and extruded gasket material replaced by pyrophyllite. This unusual efficiency eventual degrades

342   as more material is subsequently extruded from the 584OF part of the pressure medium so that

343   by the 4th compression BB-1101 resembles the initial, normal TT-960-like efficiencies. The 4th

344   compression of Bi (BB-1101) produced the equation presented in Figure 6b for calibrating the

345   force vs. pressure relation applicable to the 4th compression of a composite 584OF+pyrophyllite

346   assembly relevant to the susceptibility data in Figure 7.

347   Results for the susceptibility monitoring of stoichiometric Fe_3C as a function of pressure

348   are given in Figure 7. The steep drop in the sensor signal near 6 GPa is proportional to the loss of

349   magnetic suseptibility of the Fe_3C core to the coil windings. Thus the Curie T_C drops below

350   room T at ~6 GPa (Fig. 7).

351   **Fig. 7**

352   The clear transition in magnetic properties at 6 GPa prompted us to check whether there

353   might be parallel changes in the electrical resistance with pressure. Electrical resistivity changes

354   are often encountered at structural changes. The transitions shown by Bi during pressure

355   calibration in Figure 6a are good examples of such changes. A finding of such change might

356   indicate that the transition was structural as well as magnetic. The voltage sensed across the

357   cementite is proportional to its resistance, which falls with increasing pressure as seen in Figure

358   8. Some of this fall may be attributed to sample change of shape during compression. Even so

359   there are no deviations from a smooth compression curve that would indicate that an electrical

360   resistance change occurs in parallel with the magnetic transition seen at 6 GPa in Figure 7 in

361   stoichiometric cementite. The only 'wobbles' present are associated with the overnight cessation

362   of compression twice during the 3 day experiment. There is no electrical indication of structural

363   change at T_C. This finding is consistent with a lack of any indication in the diffraction patterns of

364   Scott et al. (2001), Li et al. (2002), Wood et al. (2004), Duman et al. (2004); Prescher et al.

365   (2012), or this study (below) that any crystal structure transition is present.

Fig. 8

366   **3.3 Magneto-elastic coupling and stoichiometry**

367   Are any volume or cell parameter effects of demagnetization visible during high-

368   resolution compression at room T in a DAC? And are such effects dependent on cementite

369   composition? We showed above that the compositional impact on T_C was measurable at zero

370   pressure, but we also showed that the effect was small enough to be within the uncertainty level

371   of the determinations of T_C with pressure in Figure 7. [1 GPa uncertainty in the T_C pressure in

372   Figure 7 translates to roughly ~25-30 °C uncertainty for an average dT_C/dP of ~25-30 °C/GPa

373   that is required to have T_C drop from 187 °C at ambient pressure to room T at 6 GPa.] Thus if

374   there are to be any differences in volumetric effects with cementite composition, they may be

375   subtle.

376   Figure 9 and Table 2 show the volume and cell parameter results of our DAC

377   compressions. The compression curve of Li et al. (2002) for stoichiometric cementite in Ne is

378   given for reference. Our densely sampled compressions appear somewhat noisier than this earlier

379   work. It is possible that the inhomogeneous strain effects of sample preparation are in play in

380   Figures 9 and 10. Nevertheless there appears to be a consistent need for all the cementite

381   compositions to have a 'wrinkle' or 'jog' in their compressions at pressures of 6-7 GPa,

382   pressures very like that of the loss of ferromagnetism in stoichiometric cementite deduced from

383   the previous findings in Figure 7. The jog is expressed in the cell volume panel as the following

384   observation. Cementites below the jog in pressure are of smaller volume than Li's whereas at

385   pressures above the jog, they are of larger volume. The pressures of the jogs are indicated by

386   vertical dashed lines (red and blue). The jogs for different cementite compositions show up at

387   slightly different pressures and are more clearly expressed by variations in different cell

388   parameters. The panel for the *a* parameter variations show that the jog is most clearly expressed

389   for the Fe-saturated cementite. The panel for the *b* parameter variations shows that the jog is

390   (noisily) expressed for the graphite-saturated cementite. The volumetric expression of T_C

391   appears, therefore, to change between crystallographic axes with cementite composition. In

392   addition, T_C varies slightly (~1 GPa) in pressure at room temperature with cementite

393   composition. The graphite-saturated cementite jogs at higher pressure than the Fe-saturated

394   cementite. There is no volume discontinuity at T_C, but cementite compressibility decreases at the

395   jogs, as do the Fe-Ni and Fe-Pt Invar alloys studied by Oomi and Mori (1981a,b).

Fig. 9

396   **3.4 Cementite unit cell parameter X-T variations**

397   The abrupt increase in thermal expansion seen by Wood et al. (2004) at 187 °C

398   corresponds to the Curie T_C as determined by loss of ferromagnetism in our experiments. We

399   sought to use this volumetric phenomenon to track the Curie T_C in pressure to convince

400   ourselves that the demagnetization seen in Figure 7 was indeed the falling of cementite's Curie

401   T_C below the room temperature horizon at 6 GPa. Our approach was to monitor the T-V

402   properties of cementite at selected pressures and look for the T at which thermal expansion

403   jumps.

404   There are a number of unusual features of the cementite unit cell response to composition

405   and temperature changes. Petch (1944) demonstrated that cementite's ambient cell parameters

406   change in a small, systematic, but complex way for samples saturated with γ-Fe quenched from a

407   range of temperatures. These cell parameter variations were thought to reflect compositional

408   changes in a range of cementites compatible with changes in the saturation level of C with T in

409   γ-Fe-saturated material grown at a range of temperatures. Walker et al. (2013) confirmed that

410   these complex variations exist and that the unit cell volume increases with C content. Indeed

411   both Petch (1944) and Walker et al. (2013) found that increase of cell volume did not occur

412   through expansion of all three axes of the orthorhombic cell of ferromagnetic cementite. The

413   studies used different settings but show the same result. By reference to the Pnma setting used by

414   Walker et al. (2013), the ***b*** axis length ***decreases*** as cell volume increases (as C content

415   increases). The ***b*** axis in this setting corresponds to the spacing between the ridge poles of the

416   pleated sheets of Fe which are the basis of the cementite structure shown in Figure 4. Shrinking

417   ***b,*** as cell volume grows with C content, implies that the pleat amplitude increases and the acute

418   angle (φ in Figure 4) between the pleats decreases with C content.

419   Wood et al. (2004) also used the Pnma setting in their study of thermal expansion of

420   cementite. In contrast to the cell expansion by C-addition at constant (quenched) T reviewed by

421   Petch (1944) and Walker et al. (2013) in which the b parameter shrinks as the cell expands, it is

422   the a parameter that shows the unusual, antithetic variation with thermal expansion at constant

423   composition. In the Pnma setting, the a parameter corresponds to the separation distance between

424   the pleated layers of Fe. ***Evidently the mechanisms of compositional and thermal expansion***

425   ***are quite different in detail as they lead to <u>different</u> axes showing anomalously constrictive***

426   ***behavior during expansion.*** Below the Curie T_C, the pleated sheet separation distance, a, in

427   ferromagnetic cementite ***decreases*** in a smooth but irregular manner as temperature and cell

428   volume increase. Wood et al. (2004) show in particular that this volume expansion, with

429   anomalous a parameter contraction, operates in the near-absence of pleat flexing. The decrease

430   in sheet separation distance, a, is particularly pronounced just below T_C. Above T_C,

431   nonferromagnetic cementite expands all its unit cell parameters, with the result that volume

432   expansion becomes larger in demagnetized cementite, and becomes larger quite abruptly. This

433   reversal of the a contraction, to become expansion of a above T_C, is an excellent XRD marker

434   for T_C and for the end of ferromagnetism with its attendant volume magnetostriction. This fact

435   explains why we pay special attention to the variation of the a cell dimension as well as the total

436   volume, in looking for a marker of T_C by XRD methods in a thermal expansion experiment at

437   each selected pressure. The volume change is diluted by the competing effects of changes in a, b,

438   and c, all stirred together during cell refinement from multiple reflections. So attention to a,

439   separately determined from the (200) cementite peak, renders T_C most clearly visible by XRD

440   methods.

441   The values of a for the cementite, from separately measured $d_{(200)}$, are shown grouped by

442   pressure in Figure 10A, along with the cell volumes from full refinement in Figure 10B. Full unit

443   cell parameters from multiple peak refinement are also given Table 3.

Fig. 10

444   Each thermal expansion cycle, except for the highest pressure cycle near 9 GPa, shows

445    $d_{(200)}$ with breaks of slope to higher slope with higher temperature. This is the T_C transition that

446   we seek, as demonstrated by Wood et al. (2004) at zero pressure. It is clear that this transition

447   appears at progressively lower temperatures with increasing pressures until the transition slips

448   beneath the room temperature horizon somewhere between the run cycles at 5 and 9 GPa, in full

449   accord with our demagnetization in a multianvil result shown in Figure 7 and with the

450   determination of Gao et al. (2008). 50-60 GPa is not needed to effect demagnetization of

451   cementite at room temperature. Vocadlo et al (2002) and Ono and Mibe (2010) predicted a

452   transition from ferromagnetic to non-magnetic state at 50-60 GPa where iron loses it local

453   magnetic moment and transforms from high-spin to low-spin state. Our results show that at 300

454   K demagnetization through a loss of magnetic ordering near 6 GPa precedes that of local

455   moment collapse at much higher pressures. The temperature progression of T_C to lower

456   temperature with higher pressure is regular and shown in Figure 11. The downward trend in T_C

457   based on the (200) peak is also shown by the full volume refinement based on all peaks in Figure

458   10B, but it is noisier and shows a more pronounced steepening of slope approaching 6 GPa. This

459   may be seen in Figure 11 as the green circles and green dashed line. We believe that the trends

460   based on the (200) peak alone are more representative of the transition than the full refinement

461   which blurs the sharp signal in a, for the reasons given above.

Fig. 11

462   There are some interesting problems with the combined information of Figures 9 and 10

463   and Tables 2 and 3. The first of these is that the T_C determined in the zero pressure DAC in these

464   two figures does not agree with that determined on ostensibly the same material, HX-26, on the

465   bench in Figure 3a. The disagreement is not large but it is measurable. The disagreement shows

466   up in Figure 11 as the mismatch of the blue, green, and orange zero-pressure points. Perhaps the

467   thermal expansion jump measured by XRD may not exactly correspond to the sharp drop in

468   susceptibility measured magnetically? If so then the magnetic T_C is expected to be higher than

469   the XRD signal, as we observe, and as is consistent with the difference between Wood et

470   al's.(2004) high quoted magnetic T_C in their abstract and the lower diffraction results in their

471   Figures. Our way of reporting magnetic T_C at the inception of the drop in susceptibility may

472   underestimate its value compared to other investigators picking some half-height of the drop as a

473   measure of T_C. Our reporting should reduce any internal discrepancy between our two

474   techniques. And still we see a resolvable difference between our XRD and magnetic signals for

475   stoichiometric HX-26. A second feature of interest is that the two thermal expansion cycles near

476   5 GPa give only slightly different T_C but resolvably different values of $d_{(200)}$ at comparable T.

477   [The full volume refinements are not resolvably different.] A third feature of interest is that the

478   slopes in the magnetic, low temperature parts of the various cycles are very different from each

479   other. For instance the zero pressure cycle has a low positive slope for the ferromagnetic portion,

480   whereas the lower-volume cycle at 4.9 GPa has a strongly negative slope in the magnetic region.

481   These slopes in the ferromagnetic region swing from plus to minus without pattern in pressure.

482   Likewise the thermal expansion slope of the paramagnetic phase does not show uniformity in

483   pressure, except to remain positive.

484   We believe these anomalies may have a common cause. We noted above that the

485   magnetization properties like T_C of alloys in the Fe-Pt and Fe-Pd system were very sensitive to

486   the annealing state of the material (Wijn, 1991; Vlaic and Borzo, 2010). T_C can easily vary by

487   150 °C in these systems according to whether the material is annealed or not. T_C may either

488   increase or decrease with annealing. If similar considerations also apply to Fe-C, then it is

489   perhaps unsurprising that the results in Figures 9 and 10 are showing some ragged behavior. This

490   is because the highly annealed state of the HX-26 cementite in Figure 3 has been degraded by

491   sample preparation for the experiments of Figures 9 and 10 by gentle crushing and then mashing

492   into a fine-grained, compact foil for DAC XRD measurements. Strains may well be present and

493   may not be homogeneous from place to place within the DAC samples, and therefore are

494   potentially different from cycle to cycle. Nakajima (1964) has documented explicitly the strong

495   effect that a few hours annealing has on the values of T_C and on the thermal expansion jump at

496   T_C of Invar Fe-Pt alloys. Given the possible magnitude of the effect of unrelieved strains on

497   magnetic and unit cell properties, and the likelihood of there being some such strains present in

498   our DAC experiments through necessary sample preparations, it is perhaps surprising that any

499   systematics, however imperfect like the data in Figures 9 and 10, survive at all!

500   Any strains introduced during DAC sample fashioning did not completely compromise

501   Curie T_C measurements but they may have introduced some noise. Although the compositional

502   impact on T_C was measurable at zero pressure, the effect was small enough to be within the

503   uncertainty level of the thermal expansion determinations of T_C with pressure. Moreover, the

504   spacing of the selected pressures of the thermal expansion cycles presented was sparse, as

505   imposed by limits of beam time and resources. And still, clear anticorrelations between T_C and

506   pressure emerge. Furthermore the trend seen plausibly connects the extremes of 0 and 6 GPa

507   (orange squares in Figure 11) that were determined magnetically on well annealed material. The

508   high-resolution compression measurements presented earlier suggest that any differences in

509   volumetric effects with cementite composition are subtle. Never the less, the effect of

510   demagnetization on compressibility suggests the reality of magnetoelastic coupling.

511   In Figure 11 the boundary between ferromagnetic cementite and non-ferromagnetic

512   cementite is drawn with a slight increase of the negative slope of the boundary beyond 3.5 GPa.

513   Given the raggedness of the blue points just discussed (and possibly assigned to strain effects), a

514   sharp kink is not really resolvable although it is more pronounced in the full volume refinement

515   data. But it seems difficult to avoid the conclusion that the dT_C/dP slope of the boundary must

516   become more negative with pressure if the T_C at 6 GPa is room T. We return to this point in later

517   discussion.

518   **3.5 dT_C/dP and Ehrenfest's second relation**

519   We showed above in Figures 9 and 10 that there are no discontinuities of volume

520   between cementite forms at T_C, just changes in the thermal expansion and compressibility,

521   consistent with the expectation that magnetic transitions are not first order. We take as a

522   corollary that there should also be no differences in the entropy (*S*) values of the forms at the

523   magnetic transition, nor of the Gibbs energy (*G*) values of forms at equilibrium. We also take as

524   a given that forms that convert rapidly to one another without hysteresis at temperatures of ~200

525   °C do so without partitioning of C. [This is the a partially constrained equilibrium of the right

526   side of Figure 5.] The ferromagnetic and non-ferromagnetic cementites must have the same

527   composition (X_C), entropy (*S*), and Gibbs energy (*G*) values as each other at the transition,

528   whether they are stoichiometric or not. Those *S* (and *G*) values change with stoichiometry (and

529   T_C) but both forms of cementite must have the same X_C, S (and G) as each other at whatever T_C

530   is appropriate. Given these conditions for a second order transition, we cannot use the Clausius-

531   Clapeyron equation to track the transition but must instead use Ehrenfest's second relation

532   (1933):

533 $$dT_C/dP = \Delta\beta/\Delta\alpha$$

534   to examine the rise or fall of T_C with pressure. $\Delta\beta$ and $\Delta\alpha$ are the changes in compressibility and

535   thermal expansion respectively at T_C. Because the thermal expansion jumps from near zero or

536   negative to positive at T_C (Wood et al., 2004), $\Delta\alpha$ is large and positive. In contrast,

537   compressibility drops modestly from the ferro- to paramagnetic cementite so $\Delta\beta$ is negative.

538   Thus the negative sign of our dT_C/dP transition in Figure 11 is consistent with our α and β in

539   Figures 8 and 9. The values observed for dT_C/dP in Figure 11 are within the range permitted by

540   the substantial variations in α and β found experimentally. Taking average thermal expansions

541   and compressibility from these figures, dT_C/dP is computed to be ~30±20 K/GPa as given in

542   Table 4. On average this would give 180 K drop for 6 GPa pressure which accords nicely with

543   our independent determination that the 1 bar T_C of 187 °C drops below room T by application of

544   6 GPa of pressure (Figure 7).

545   It is unusual to have a phase transition in which the phase on the high pressure side has

546   the larger thermal expansion. Usually the higher density phase at higher pressure has lower

547   thermal expansion, and is also less compressible. The paramagnetic cementite at high pressure is

548   observed to be less compressible, as expected under normal conditions for first order phase

549   transitions. But this is a second order transition, and the high pressure cementite does not have a

550   higher density at the transition – the volumes are the same! Thus the normal expectations for

551   compressibility are reached *in spite* of the normal baseline conditions of density increase not

552   being met. There are exceptions to the expectation that thermal expansion commonly drops when

553   density increases. Walker et al. (2002) showed that both KCl and RbCl *increased* their thermal

554   expansion by transforming to the high density, high pressure forms. Coordination number

555   increases in the high pressure forms overcome polarization effects that artificially lower

556   interionic distances in the low pressure forms. This time cementite confounds the 'normal'

557   expectation for thermal expansion *in spite of* the fact that it has no coordination changes or spin

558   transitions to invoke to get a pass from the expectation of falling thermal expansion with

559   pressure. In this case the magnetovolume effect within the ferromagnetic phase artificially keeps

560   thermal expansion below values for the paramagnetic high pressure phase. Given all this contrary

561   behavior, it is reassuring that there is acceptable congruence between dT_C/dP and $\Delta\beta/\Delta\alpha$.

562   The rate of descent of T_C between 0 and 3.5 GPa is about 14 °C/GPa, which is about the

563   same drop in just the first GPa as experienced for the whole stoichiometric range stably

564   accessible at ambient P. Figure 11 also shows that the descent of T_C with P in the interval 3.5-6

565   GPa increases to ~50°C/GPa. Although we remarked earlier that a kink at 3.5 GPa is not really

566   resolvable (compared to a continuous increase in the rate of descent of T_C with P), an increase in

567   descent rate makes sense. Without phase changes or magnetic or spin transitions, thermal

568   expansions and compressibilities should both decrease with pressure and phase density.

569   Depending on which shrinks faster, the rate of change of T_C could increase or decrease. However

570   thermal expansion in the ferromagnetic cementite anomalously shrinks less than it might because

571   of magnetostriction. Thus the magnitude of $\Delta\alpha$ is expected to anomalously diminish and the drop

572   rate of T_C to increase. This is indeed marginally observed. Leger et al. (1972) suggested that for

573   Invar-type materials with weak interaction that the drop in T_C should be parabolic in P. The inset

574   within Figure 11 shows the data based on d_{200} recast parabolically. The d_{200} data do, very

575   roughly, approximate a parabolic fit.

576   It is curious that the C-rich cementite should lose ferromagnetism at a higher pressure

577   than either the C-deficient (DAC determination, Figure 9) or the stoichiometric (MA

578   determination, Figure 7) cementites. It is curious because both off-stoichiometry cementites have

579   lower T_C than stoichiometric cementite at ambient P. They might be expected to transform at

580   lower pressure than the stoichiometric material, if one assumes that all cementites have the same

581   dT_C/dP for the transition. We do not have a high resolution compression of stoichiometric

582   material for direct comparison to Figure 9 to determine whether the stoichiometric material

583   transforms at a higher P, but Figure 7 suggests otherwise. And we certainly have no assurance

584   that all cementites have the same dT_C/dP. There is a rich field of possibilities for further

585   experimental observation.

586   **3.6 Implications for cementite stability**

587   Gao et al. (2008) also show loss of magnetism in stoichiometric cementite by an

588   independent technique, synchrotron Mössbauer, within the pressure interval between 4.3 and 6.5

589   GPa – a pressure interval that does include 6 GPa and does not include 60 GPa. Ferromagnetic

590   stability of cementite is limited to 6 GPa, not 60 GPa. The Mössbauer work of Prescher et al.

591   (2012) apparently puts the demagnetization pressure for cementite slightly higher than ours or

592   Gao's, nearer to 10 GPa, but it should be noted that their sextets are no longer resolvable by 7.5

593   GPa, suggesting that ferromagnetism may indeed be gone at considerably less than 10 GPa.

594   Furthermore it is very likely that their synthesis method gives C-excess cementites, which we

595   have seen lose their magnetism at slightly higher pressures than C-deficient ones, so there may

596   be no serious discrepancy with our results. Likewise Duman et al. (2005) give a ~10 GPa

597   pressure for demagnetization determined by X-ray magnetic circular dichroism (XMCD), but

598   again on a specimen likely to be C-excess, that is further complicated by being 50 nm in grain

599   size. All these experimental determinations agree that ferromagnetism is lost in cementite by 10

600   GPa, if not by 6 GPa, and that ferromagnetism does not continue to near half a megabar.

601   However Prescher et al. (2012) identified another transition near 22GPa that they assigned to

602   spin reducing the paramagnetic state to nonmagnetic. Likewise Lin et al. (2004) found that X-ray

603   emission spectroscopy indicated a loss of magnetism at a very similar pressure of ~25 GPa.

604   These studies explore magnetism loss by a spin mechanism other than the ferro- to paramagnetic

605   transition. Neither study is comparable with the theoretical estimates of 50-60 GPa for loss of

606   cementite magnetism by spin drop (which does not consider paramagnetism), or the several

607   experimental determinations that the loss of ferromagnetism to paramagnetism happens below 10

608   GPa.

609   What difference does the 6 (or 10) GPa to 60 GPa interval make for the calculation of the

610   even higher pressure stabilities of the carbides? This ~half megabar pressure run for integrating

611   V·dP, to find a pressure effect on cementite *G*, and thus on carbide stability, is not a trivial P

612   interval. If the ferromagnetic equation of state is used through this interval, with its larger

613   compressibilities, the volumes and attendant additions to *G* at pressure will be too small. *G* will

614   not be sufficiently raised in P to reflect reality. *G* will be lower than it ought to be, with the

615   consequence that cementite stability will appear artificially high with respect to other possible

616   states of the system, for example Fe + carbon or Fe + some other carbide like the Eckstrom-

617   Adcock carbide, Fe_7C_3. Cementite ferromagnetism's early demise at high pressure has as a

Revision 1 *American Mineralogist* June 2015   29

618   consequence a more restricted potential stability for cementite itself at pressures even higher than

619   those of the magnetism's demise.

620   **4 Concluding remarks**

621   The effect of pressure on the Curie temperature (T_C) of cementite was determined both

622   directly, by monitoring the magnetization as a function of pressure, and indirectly, by observing

623   changes in the thermal expansion at a range of pressures. T_C for stoichiometric Fe_3C cementite

624   was found to fall parabolically with pressure from 187 $^\circ$C at ambient pressure to room

625   temperature at 6 GPa. Non-stoichiometric cementite T_C also falls with pressure with both

626   increase and decrease in carbon content. The pressures at which T_C drops to ambient in carbon-

627   saturated and Fe-saturated cementite were found to be ~7 GPa and ~6 GPa respectively. The

628   drop in T_C with composition of cementite at ambient pressure is small and asymmetric about the

629   stoichiometric composition being steeper on the carbon excess side. Neither X-ray diffraction

630   nor electrical conductivity measurements provided any evidence for a structural phase transition

631   with the loss of magnetism. Pressure, temperature, and composition are found to affect the

632   crystal structure differently leading to a complex relationship with T_C.

640   05CH11231. We thank two anonymous reviewers for their constructive comments. LDEO

641   contribution ####.

642   **References**

643   Birch F. (1986) Equation of state and the thermodynamic parameters of NaCl to 300 kbar in the

644   high-temperature domain. *Journal of Geophysical Research,* **91**, 4949-4954.

645   Buono A, 2011, High Pressure Melting of Iron with Nonmetals Sulfur, Carbon, Oxygen, and

646   Hydrogen: Implications for Planetary Cores, PhD Dissertation, Columbia University, Ch.

647   3, 50-80.

648   Buono AS, R Dasgupta, C-TA Lee, D Walker (2013) Siderophile element partitioning between

649   cohenite and liquid in the Fe–Ni–S–C system and implications for geochemistry of

650   planetary cores and mantles. Geochimica et Cosmochimica Acta 120 (2013) 239–250,

651   http://dx.doi.org/10.1016/j.gca.2013.06.024

652   Cheary, R.W., and Coelho, A.A. (1996) Programs XFIT and FOURYA, deposited in CCP14

653   powder diffraction library. Engineering and Physical Sciences Research Council,

654   Daresbury Laboratory, Warrington, England.

655   Chen, B., L. Gao, B. Lavina, P. Dera, E. E. Alp, J. Zhao, and J. Li (2012), Magneto-elastic

656   coupling in compressed Fe_7C_3 supports carbon in Earth's inner core, Geophys. Res. Lett.,

657   39, L18301.

658   Chen B., Li Z., Zhang D., Liu J.C., Hu M.Y., Zhou J., Bi W., Alp E.E., Xioa Y., Chow P., Li J.

659   (2014) Hidden carbon in the Earth's inner core revealed by shear softening in dense Fe_7C_3.

660   PNAS, www.pnas.org/cgi/doi/10.1073/pnas.1411154111

661   Dasgupta R, 2013, Ingassing, storage, and outgassing of terrestrial carbon through geologic time.

662   Rev. Mineral. Geochem., 75, 183-229. doi:10.2138/rmg.2013.75.7

663   Dasgupta R and Hirschmann M, 2010, The deep carbon cycle and melting in the Earth's interior.

664   Earth Planet. Sci. Lett., 298, 1-13.

665   Dasgupta, R., Walker, D., 2008. Carbon solubility in core melts in a shallow magma ocean

666   environment and distribution of carbon between the Earth's core and the mantle.

667   Geochimica et Cosmochimica Acta 72, 4627-4641.

668   Dasgupta, R., Buono, A., Whelan, G., Walker, D., 2009. High-pressure melting relations in Fe-

669   C-S systems: Implications for formation, evolution, and structure of metallic cores in

670   planetary bodies. Geochimica et Cosmochimica Acta 73, 6678-6691.

671   Duman E., Acet M., Hülser T., Wassermanm E.F., Rellinghaus B., Itié J.P., and Munsch P

672   (2004) Large spontaneous magnetostrictive softening below the Curie temperature of Fe_3C

673   Invar particles. J. Appl. Phys., 96, 5668-5672.

674   Duman E., M. Acet, E. F. Wassermann, J. P. Itié, F. Baudelet, O. Mathon, and S. Pascarelli

675   (2005) Magnetic Instabilities in Fe_3C Cementite Particles Observed with Fe *K*-Edge X-

676   Ray Circular Dichroism under Pressure, Phys. Rev. Lett. 94, 075502

677   Ehrenfest P (1933) Phasenumwandlungen im ueblichen und erweiterten Sinn, classifiziert nach

678   den entsprechenden Singularitaeten des thermodynamischen Potentiales. Proceedings

679   Koninklijke Nederlandse Akademie van Wetenschappen, 36, d.2, 153-157.

680   Gao L, Chen B, Wang JY, Alp EE, Zhao JY, Lerche M, Sturhahn W, Scott HP, Huang F, Ding

681   Y, Sinogeikin SV, Lundstrom CC, Bass JD, Li J, 2008, Pressure-induced magnetic

682   transition and sound velocities of Fe$_3$C: Implications for carbon in the Earth's inner core.

683   Geophys. Res. Lett, 35, L17306.

684   Gao, L., Chen, B., Zhao, J., Alp, E.E., Sturhahn, W., Li, J., 2011. Effect of temperature on sound

685   velocities of compressed Fe$_3$C, a candidate component of the Earth's inner core. Earth and

686   Planetary Science Letters 309, 213-220.

687   Hammersley, A.P., Svensson, S.O., Hanfland, M., Fitch A.N., and Häusermann, D. (1996) Two-

688   dimensional detector software: from real detector to idealised image or two-theta scan.

689   High Pressure Research, 14, 235-248

690   Laugier J and B Bochu (2003) CELREF v3, Freeware from Http://www.inpg.fr/LMGP

691   Leger JM, Loriers-Susse C, and Vodar B (1972) Pressure effect on the Curie temperatures of

692   transition metals and alloys. Phys. Rev. B 6, 4250-4261.

693   Li J, Mao HK, Fei Y, Gregoryanz E, Eremets M, and Zha CS (2002) Compression of Fe$_3$C to 30

694   GPa at room temperature, Phys. Chem. Min. 29, 166-169.

695   Lin JF, Struzhkin VV, Mao H-K, Hemley RJ, Chow P, Hu MY, Li J (2004) Magnetic transition

696   in Fe$_3$C from X-ray emission spectroscopy. Phys. Rev. B, 70, 212405.

697   Lord OT, Walter MJ, Dasgupta R, Walker D, Clark SM, 2009, Melting in the Fe-C system to 70

698   GPa. Earth and Planetary Science Letters 284, 157-167

699   Mookherjee M, 2011, Elasticity and anisotropy of Fe$_3$C at high pressures. Amer. Min., 96, 1530-

700   1536.

701   Mookherjee M, Nakajima Y, Steinli-Neumann G, Glazyrin K, Wu X, Dubrovinski L,

702   McCammon C, Chumakov A, 2011, High pressure behavior of iron carbide (Fe$_7$C$_3$) at

703   inner core conditions. Jour. Geophys. Res., 116, B04201, doi:10.1029/2010JB007819

704   Nakajima T (1964) Effect of pressure on the Curie temperature in Invar-type Iron-Platinum

705   alloys as a phase transition of the second kind, Jour. Physical Soc. Japan, 19, 520-529.

706   Nakajima, Y., Takahashi, E., Suzuki, T., Funakoshi, K.I., 2009. "Carbon in the core" revisited.

707   Phys. Earth Planet. Inter. 174, 202–211

708   Nakajima Y, Takahashi E, Sata N, Nishihara Y, Hirose K, Funakoshi K, Ohishi Y, 2011,

709   Thermoelastic property and high pressure stability of Fe_7C_3: implications for iron-carbide

710   in the Earth's core. Am. Miner., 96, 1158-1165.

711   Ono, S., Mibe, K., 2010. Magnetic transition of iron carbide at high pressures. Phys. Earth

712   Planet. Inter. 180, 1–6.

713   Oomi G. and Mori N. (1981a) Bulk modulus anomalies of Fe-Ni and Fe-Pt Invar alloys. Jour.

714   Physical Soc. Japan, 50, 2917-2923.

715   Oomi G. and Mori N. (1981b) Pressure effect on the spontaneous volume magnetostriction of

716   Fe-Ni and Fe-Pt Invar alloys. Jour. Physical Soc. Japan, 50, 2924-2930.

717   Petch NJ (1944) The interpretation of the crystal structure of cementite. J Iron Steel Inst

718   149:143–150

719   Prescher C., L. Dubrovinsky, C. McCammon, K. Glazyrin, Y. Nakajima, A. Kantor, M. Merlini,

720   and M. Hanfland (2012) Structurally hidden magnetic transitions in Fe_3C at high

721   pressures, Phys. Rev. B 85, 140402(R)

722   Scott, H. P., Williams, Q. & Knittle, E. (2001). Stability and equation of state of Fe_3C to 73 GPa:

723   Implications for carbon in the Earth's core. Geophys. Res. Lett. 28, 1875-1878.

724   Vlaic P and E Burzo (2010) Magnetic behavior of iron-platinum alloys, J. Optoelectronics and

725   advanced materials, 12, 1114-1124.

Revision 1 *American Mineralogist* June 2015   34

726   Vŏcadlo, L., Brodholt, J., Dobson, D.P., Knight, K.S., Marshall, W.G., Price, G.D., Wood, I.G.,

727   2002. The effect of ferromagnetism on the equation of state of Fe_3C studied by first-

728   principles calculations. Earth Planet. Sci. Lett. 203, 567–575.

729   Walker D, Carpenter MA, Hitch CM, 1990, Some simplifications to multi-anvil devices for high

730   pressure experiments. Amer. Min., 75, 1020-1028.

731   Walker D, R. Dasgupta, J. Li, and A. Buono (2013) Nonstoichiometry and growth of some Fe

732   carbides. Contrib. Min. Pet., 166:935-957, DOI 10.1007/s00410-013-0900-7

733   Wijn HPJ ed. (1991) Magnetic properties of metals, d-elements, alloys and compounds. in Data

734   in Science and Technology, R Poerschke Ed in Chief, Springer-Verlag, p. 86, fig 29, 30.

735   Winterrose ML, Lucas MS, Yue AF, Halevy I, Mauger L, Muñoz JA, Hu J, Lerche M, and Fultz

736   B (2009) Pressure-induced Invar behavior in Pd_3Fe, Phys. Rev. Lett., 102, 237202, 1-4.

737   Wood, B.J., 1993. Carbon in the core. Earth and Planetary Science Letters 117, 593-607

738   Wood IG, L Vŏcadlo, KS Knight, DP Dobson, WG Marshall, GD Price. and J Brodholt, (2004)

739   Thermal expansion and crystal structure of cementite, Fe_3C, between 4 and 600 K

740   determined by time-of-flight neutron powder diffraction Journal of Applied

741   Crystallography, ISSN 0021-8898. 37, 82-90. DOI: 10.1107/S0021889803024695

742   **Figure captions**

743   **Figure 1 (a)** Irregular half-cylinder ingot (axis horizontal) of stoichiometric Fe_3C cementite

744   (HX26) slightly tarnished after room P determination of Curie T_C in air. Surface wrinkles

745   were inherited from the enclosing Al_2O_3 cylindrical encapsulation used in the piston-cylinder

746   synthesis. **(b)** after subsequent multianvil pressurization and recovery by dissolution of

747   encapsulating KBr. The same original surface wrinkles still identifiable, indicating that the

748   KBr encapsulation was effective at resisting the normal mashing inherent in multianvil

749   compressions. Mm scale spacing between ruled tick marks on substrate. **(c)** Configuration of

750   coiled windings used to detect magnetic susceptibility of contents. Preliminary version on Cu

751   form used to measure T_C for a variety of cementite compositions within a non-inductively

752   wound resistance furnace [not shown]. The 1" steel finishing nail provides the scale and was

753   used as a magnetic test piece for circuit tuning before ingot insertion. **(d)** Revised epoxy

754   impregnated version on an MgO form (0.312" OD) for insertion into a 12 mm TEL octahedral

755   multianvil assembly along a [110] edge-to-edge direction. Coil leads through the octahedral

756   gaskets proved to be problematic, being eventually replaced by direct contacts with truncated

757   WC cube faces, which then formed part of the activation and detection circuits. **(e)** Multianvil

758   assembly for magnetic susceptibility detection at pressure. **(f)** Bi pressure calibration

759   assembly. Unusual features of these assemblies in **e** and **f** are the use of vacuum-epoxy-

760   impregnated internal induction coils (Figure 1e), KBr encapsulation of Fe_3C in BB-1091, and

761   multiple compressions of the 584OF (Aremco) castable ceramic pressure media in both

762   experiments. The first compression of each experiment series employed integral 584OF

763   gaskets which disintegrate during unloading. Compressions subsequent to the first were

764   gasketed by the addition of cut pyrophyllite gaskets to substitute for the previously

765   disintegrated gaskets.

766   **Figure 2 (A)** Diamond anvil cell (DAC) on ALS end station 12.2.2 showing principal features of the

767   installation used in this study. Two typical image plate records show the first loading of the Fe-saturated

768   compression and the last image of the stoichiometric thermal expansion run. Even smudgy images with

769   preferred orientation indications like all those of the HX26run7 series integrate nicely as shown in **(B)** of

770   the stack of selected 1D images of the thermal expansion HX26run 7. The larger thermal expansion of

771   NaCl is shown by the greater 2 theta shifts in peak locations with temperature. Cementite (hkl) given in

772   boxes. Unlabeled peaks are NaCl (111), (200), and (220).

773   **Figure 3 (A) and (B)** Secondary coil AC voltage as a function of sample temperature as recorded from

774   sensor shown in Figure 1c. Abrupt drops in this voltage signal the Curie T_C where the cementite loses

775   ferromagnetism. Hopkinson's maximum is poorly developed before the abrupt plunge, suggesting the

776   absence of blocking effects. Stoichiometric cementite shown in A has a higher T_C than nonstoichiometric

777   compositions shown in B. **(C)** Summary of ambient pressure determinations of cementite Curie T_C from

778   Figure 3AB as a function of cementite bulk composition. Stoichiometric Fe_3C cementite HX-26 has the

779   highest Curie T_C whereas both graphite-saturated and Fe-saturated cementites have ~13-14 °C lower

780   Curie T_C. Intermetallic solutions of Fe-Pt and Fe-Pd also show maximum Curie T_C at stoichiometric

781   compounds, e.g. FePt, FePd, and $FePd_3$, but at higher T_C. The Curie T_C of these alloys in the literature

782   was found to vary by as much as 150 °C depending on annealing state (Wijn, 1991).

783   **Figure 4.** Cementite structure shown in two projections. The upper projection along *c* onto the ***a-***

784   ***b*** plane looks along the ridgepoles and valleys that flex the hexagonal Fe layers into pleats. Fe

785   atoms are the large orange symbols and C atoms are the small black symbols close to the flexural

786   ridgepoles and valleys. The angle ϕ is the acute angle of the pleating. The lower projection along

787   *a* onto the ***b-c*** plane has dashed lines indicating the ridgepoles and valleys of the pleats in the Fe

788   layers. There are twice as many unoccupied potential C sites between the ridgepoles and valleys

789   as there are occupied C sites [at stoichiometric Fe_3C] associated with the pleat flexures.

790   **Figure 5** Notional form of $G(X_C)$ curves (*G* is Gibbs energy) for ferromagnetic (red) and paramagnetic

791   (blue) cementite at temperatures below and above T_C for stoichiometric Fe_3C. For the lower temperatures

792   (upper curves), there are two intersections which correspond to off-stoichiometric Curie T_C - both are

793   lower T_C than that for stoichiometric Fe_3C. The C-poor one is farther from Fe_3C than the C-rich one. For

794   the lower dashed curves T is too high for stable magnetic ordering at any composition and all cementites

795   are paramagnetic. By arbitrary choice the C-rich branch is drawn for constrained equilibria where C

796   cannot move, whereas the C-poor branch arbitrarily allows for C partitioning, raising the possibility of a

797   loop in more kinetically favorable circumstances.

798   **Figure 6 (a)** Millivolts detected across a Bi cylinder by 4 wire circuit activated by a 15 VDC signal in

799   series with a 150 ohm resistor as a function of press force. The Bi cylinder (1.4 mm diameter x 4 mm

800   long) changes resistance in response to phase changes between Bi I, Bi II, Bi III, and Bi V as a result of

801   pressurization at room temperature. The relation between pressure and force (in US tons) for these and

802   related experiments is given in Figure 6b. **(b)** Pressure of sample vs. (US) tons force in press

803   calibrations. Experiment TT-960 uses a normal 584OF pressure medium and gasket without epoxy

804   impregnation. This LDEO run is shown for reference and has a Bi III-V transition pressure (425 tons) that

805   is indistinguishable from the average of 7 Bi III-V calibrations (429±18 tons) done at the University of

806   Michigan. The other 3 BB experiments are epoxy-impregnated, pyrophyllite-gasketed retreads from an

807   initial compression that failed. We use the equation given for the quadratic fit to the 4th compressive cycle

808   data (BB-1101) to assign pressures to the compressive forces applied to the Fe_3C in experiment BB-1091

809   (also 4th cycle) that monitors Fe_3C magnetic susceptibility in Figure 7.

810   **Figure 7** Microvolts AC sensed on secondary pickup coil as a function of HX-26 Fe_3C sample pressure

811   in 4th compression experiment BB-1091; calibrated in pressure by 4th cycle Bi experiment BB-1101.

812   **Figure 8** Millivolt signal on a 4 wire circuit activated by a 0.1 amp current across a cylinder of HX-26

813   stoichiometric cementite between Al electrodes as a function of multianvil compression in experiment

814   TT-904. Minor offsets of the trace correspond to pauses in the compression cycle during which the

815   pressure drifted with little change in the mV signal.

816   **Figure 9** Volumetric properties of cementites with compression to ~10 GPa at ambient T. The volumes

817   and *c* parameters of nonstoichiometric cementite agree fairly well with those of stoichiometric cementite

Revision 1 *American Mineralogist* June 2015   38

818   given by Li et al. (2002). However there are obvious differences between the *a* and *b* parameters in that

819   study and this one. The *a* parameters in this study are systematically smaller than those of Li et al. (2002).

820   Our *b* parameters are systematically larger. This is the case irrespective of cementite composition. The

821   volumes of our cementites appear to take a 'jog' in the 6-7 GPa region, near T_C. The jog for Fe-saturated

822   cementite HX-39 commences about 6 GPa (vertical dashed red line), the same ambient Tc determined for

823   stoichiometric cementite in Figure 7. The jog for graphite-saturated HX-32 is nearer 7 GPa (vertical

824   dashed blue line). The Fe-saturated composition expresses this change most clearly in the pressure

825   variation of the *a* parameter, whereas the graphite-saturated cementite shows this change most clearly in

826   the *b* parameter. The jogs are not discontinuities in cell volume or cell parameter, but are changes of their

827   rate of change of volume with pressure (compressibility).

828   **Figure 10** A. Linear thermal expansion of the *a* parameter in HX-26 stoichiometric cementite at 6

829   selected pressures. In **A** the *a* parameter is extracted directly from the 2 theta position of the (200) peak,

830   not from the full refinement of all peaks given in Table 3. Peak position was determined by XFIT. Error

831   bars are smaller than the symbol. **B.** Volume thermal expansion of HX-26 derived from full refinement of

832   all peaks. Peaks fit with XFIT and refined with Celref 3.

833   **Figure 11** Magnetic phase diagram for stoichiometric cementite. Paramagnetic, high thermal expansion

834   (High-α) cementite is favored at both high T and high P. Ferromagnetic, low thermal expansion (Low-α)

835   cementite becomes unstable above 6 GPa at room temperature. Transition T_C based on the jump in

836   expansion shown by the (200) peak extracted from Figure 10A plotted as function of pressure as blue

837   diamonds, showing a clear trend with negative dT_C/dP. Orange squares at T-P extremes are the one bar

838   determinations of Figure 3 and the 6 GPa determination by multianvil of Figure 7 done by magnetic

839   detection of loss of ferromagnetism. The different data sets are broadly consistent with each other and

840   with the notion of ferromagnetism's T_C decreasing smoothly in temperature with pressure between the

841   orange points that are determined from actual loss of ferromagnetism. The increasingly negative dT_C/dP

842   with pressure is marginally resolvable here given the uncertainties in the blue diamonds, but it is more

39

843 pronounced in the data derived from full volume refinement of all cell parameters in figure 10B given by

844 the green circles and green dashed line. The inset figure presents the blue diamond data based on $d_{(200)}$ in

845 the parabolic form suggested by Leger et al. (1972) for Invar materials.

846 **Tables**

Table 1	Synthesis and T_C of cementites			
Material *	at. % C	phases	anneal time hrs	Curie Tc °C
HX32	26	cementite, graphite	102	174
HX26	25	cementite	96	186
HX26	25	cementite	96	187†
HX35	22.9	cementite	75.3	173
HX39	22	cementite, Fe	118	173
* From syntheses at 1 GPa, 1110 °C			†duplicate on separate piece	

847

Revision 1 *American Mineralogist* June 2015   40

Table 2												
Cementite compression at room temperature in ethanol:methanol ALS December 2012												
Fe saturated	a nacl	+/-	GPa	+/-	a	+/-	b	+/-	c	+/-	vol	+/-
hx39_001	5.6440	0.0040	-0.1	0.05	5.0764	0.0016	6.7433	0.0059	4.5170	0.0015	154.63	0.15
hx39_006	5.5196	0.0096	1.8	0.18	5.0662	0.0021	6.7278	0.0031	4.5026	0.0022	153.47	0.12
hx39_008	5.5752	0.0055	0.9	0.08	5.0736	0.0014	6.7484	0.0016	4.5056	0.0012	154.26	0.07
hx39_012	5.6040	0.0144	0.5	0.20	5.0782	0.0016	6.7492	0.0031	4.5091	0.0013	154.54	0.10
hx39_018	5.4842	0.0317	2.5	0.61	5.0573	0.0019	6.7316	0.0023	4.4950	0.0014	153.03	0.09
hx39_019	5.4603	0.0147	3.0	0.30	5.0529	0.0011	6.7234	0.0016	4.4916	0.0010	152.59	0.06
hx39_020	5.4231	0.0077	3.8	0.18	5.0428	0.0021	6.7145	0.0031	4.4860	0.0020	151.90	0.12
hx39_021	5.4035	0.0144	4.3	0.35	5.0376	0.0015	6.7018	0.0026	4.4843	0.0024	151.39	0.11
hx39_022	5.3811	0.0018	4.8	0.04	5.0337	0.0019	6.7049	0.0029	4.4822	0.0026	151.27	0.12
hx39_003	5.3799	0.0233	4.8	0.45	5.0302	0.0024	6.7022	0.0028	4.4749	0.0017	150.87	0.11
hx39_026	5.3566	0.0191	5.5	0.51	5.0248	0.0021	6.7101	0.0039	4.4708	0.0025	150.74	0.14
hx39_027	5.3440	0.0084	5.8	0.24	5.0209	0.0015	6.7009	0.0028	4.4680	0.0015	150.33	0.09
hx39_028	5.3349	0.0015	6.1	0.04	5.0184	0.0019	6.6978	0.0028	4.4640	0.0024	150.05	0.12
hx39_029	5.3203	0.0101	6.5	0.29	5.0181	0.0022	6.6935	0.0059	4.4690	0.0019	150.11	0.16
hx39_030	5.3102	0.0316	6.8	0.93	5.0174	0.0026	6.7014	0.0052	4.4648	0.0021	150.12	0.16
hx39_031	5.2977	0.0313	7.2	0.95	5.0130	0.0018	6.6930	0.0032	4.4596	0.0018	149.63	0.11
hx39_032	5.2842	0.0271	7.6	0.84	5.0096	0.0019	6.6836	0.0031	4.4628	0.0017	149.42	0.11
hx39_033	5.2665	0.0057	8.2	0.19	5.0054	0.0018	6.6746	0.0028	4.4595	0.0016	148.99	0.10
hx39_034	5.2494	0.0114	8.8	0.40	5.0013	0.0027	6.6736	0.0040	4.4576	0.0022	148.78	0.14
hx39_035	5.2327	0.0051	9.4	0.18	5.0032	0.0023	6.6649	0.0032	4.4478	0.0018	148.32	0.12
hx39_036	5.2178	0.0420	9.9	1.57	4.9995	0.0017	6.6660	0.0021	4.4490	0.0017	148.27	0.09
hx39_037	5.2021	0.0448	10.6	1.62	4.9982	0.0024	6.6582	0.0035	4.4452	0.0019	147.93	0.12
hx39_038	5.1845	0.0227	11.3	0.89	4.9989	0.0033	6.6636	0.0032	4.4493	0.0020	148.21	0.14
C saturated												
hx32_001	5.3956	0.0106	4.5	0.26	5.0502	0.0025	6.7082	0.0043	4.4707	0.0023	151.46	0.15
hx32_002	5.4174	0.0408	3.9	0.89	5.0404	0.0015	6.7040	0.0034	4.4768	0.0019	151.28	0.11
hx32_004	5.4025	0.0570	4.3	1.27	5.0424	0.0014	6.6996	0.0030	4.4789	0.0016	151.31	0.10
hx32_008	5.5987	0.0048	0.6	0.06	5.0750	0.0019	6.7274	0.0056	4.5232	0.0028	154.43	0.17
hx32_009	5.5469	0.0058	1.4	0.10	5.0673	0.0018	6.7501	0.0025	4.5166	0.0020	154.49	0.11
hx32_010	5.5102	0.0203	2.0	0.36	5.0665	0.0025	6.7368	0.0042	4.5041	0.0030	153.73	0.16
hx32_011	5.4746	0.0109	2.7	0.22	5.0553	0.0032	6.7320	0.0051	4.4972	0.0028	153.05	0.18
hx32_013	5.3805	0.0108	4.8	0.28	5.0472	0.0027	6.6884	0.0049	4.4777	0.0025	151.16	0.16
hx32_014	5.3578	0.0035	5.4	0.09	5.0344	0.0021	6.6743	0.0034	4.4751	0.0019	150.37	0.12
hx32_015	5.3143	0.0016	6.7	0.05	5.0171	0.0024	6.6773	0.0029	4.4525	0.0021	149.16	0.12
hx32_016	5.2830	0.0035	7.7	0.13	5.0102	0.0035	6.6811	0.0048	4.4460	0.0038	148.83	0.20
hx32_017	5.2602	0.0092	8.4	0.31	5.0175	0.0048	6.6686	0.0052	4.4478	0.0031	148.82	0.21
hx32_018	5.2403	0.0064	9.1	0.23	5.0047	0.0025	6.6691	0.0033	4.4501	0.0038	148.53	0.16
hx32_019	5.2233	0.0081	9.7	0.30	5.0011	0.0027	6.6688	0.0052	4.4424	0.0028	148.16	0.17
hx32_020	5.2142	0.0106	10.1	0.68	5.0036	0.0035	6.6758	0.0063	4.4387	0.0031	148.27	0.20
hx32_021	5.2442	0.0057	9.0	0.21	5.0050	0.0033	6.6837	0.0040	4.4444	0.0040	148.68	0.19
hx32_022	5.5121	0.0041	2.0	0.07	5.0818	0.0061	6.7132	0.0097	4.5163	0.0070	154.08	0.38
hx32_023	5.6317	0.0167	0.1	0.21	5.0791	0.0021	6.7555	0.0031	4.5090	0.0028	154.71	0.11

848
849

Table 3

Thermal expansion of stoichiometric cementite at selected pressures in ethanol:methanol ALS May 2013

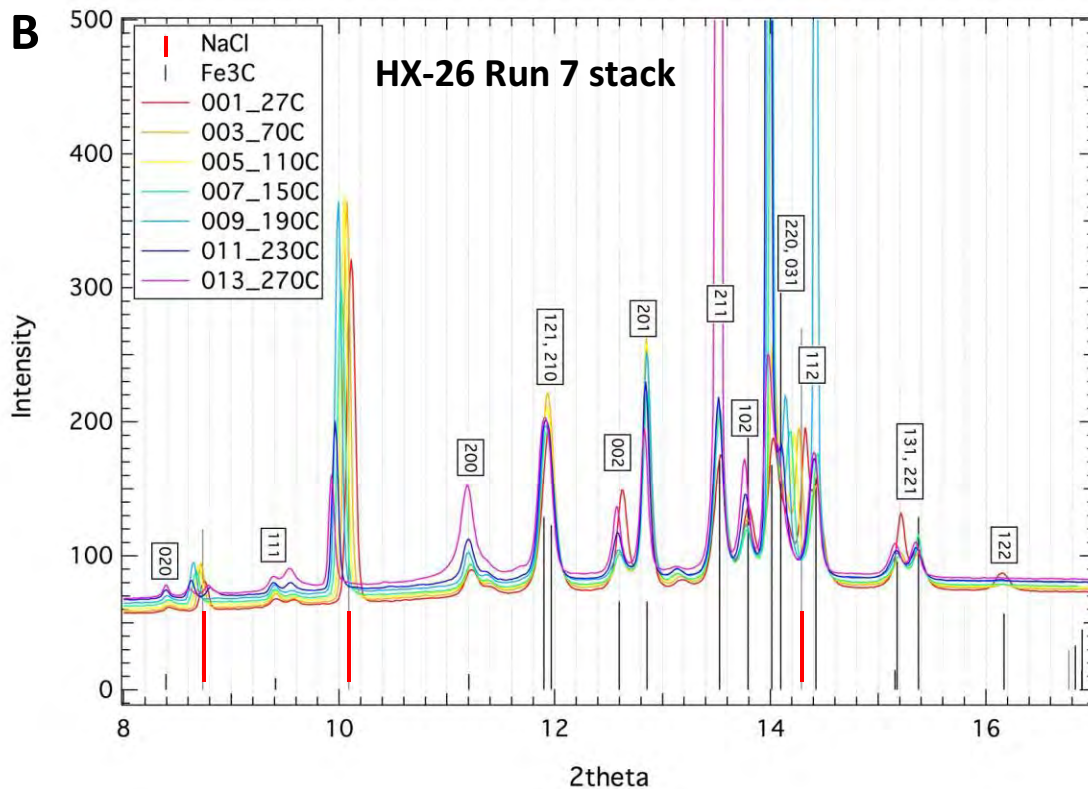|	T C	T K	NaCl a	+/-	GPa	+/-	2*d_{200}	a	+/-	b	+/-	c	+/-	vol	+/-
hx26run7_001	27	300	5.6296	0.0167	0.14	0.21	5.0678	5.0828	0.0037	6.7614	0.0070	4.5168	0.0033	155.23	0.23
hx26run7_002	51	324	5.6419	0.0059	0.05	0.07	5.0692	5.0824	0.0027	6.7615	0.0050	4.5188	0.0024	155.29	0.16
hx26run7_003	71	344	5.6475	0.0047	0.04	0.06	5.0707	5.0832	0.0028	6.7625	0.0052	4.5198	0.0025	155.37	0.17
hx26run7_004	91	364	5.6560	0.0012	-0.01	0.01	5.0732	5.0828	0.0032	6.7641	0.0059	4.5203	0.0028	155.41	0.19
hx26run7_005	110	383	5.6633	0.0072	-0.04	0.08	5.0740	5.0815	0.0023	6.7692	0.0051	4.5206	0.0020	155.50	0.15
hx26run7_006	130	403	5.6728	0.0029	-0.09	0.04	5.0732	5.0789	0.0025	6.7677	0.0045	4.5232	0.0022	155.48	0.15
hx26run7_007	150	423	5.6772	0.0100	-0.09	0.11	5.0750	5.0810	0.0022	6.7749	0.0050	4.5204	0.0020	155.61	0.15
hx26run7_008	170	443	5.6864	0.0025	-0.13	0.03	5.0760	5.0792	0.0020	6.7794	0.0036	4.5223	0.0018	155.72	0.12
hx26run7_009	190	463	5.6959	0.0066	-0.18	0.07	5.0800	5.0848	0.0018	6.7772	0.0041	4.5236	0.0016	155.89	0.12
hx26run7_010	210	483	5.7027	0.0167	-0.19	0.18	5.0830	5.0849	0.0025	6.7809	0.0056	4.5252	0.0022	156.03	0.17
hx26run7_011	230	503	5.7118	0.0045	-0.23	0.05	5.0828	5.0874	0.0019	6.7831	0.0036	4.5274	0.0016	156.23	0.12
hx26run7_012	250	523	5.7220	0.0162	-0.28	0.15	5.0850	5.0907	0.0024	6.7892	0.0054	4.5284	0.0021	156.51	0.16
hx26run7_013	270	543	5.7215	0.0287	-0.22	0.27	5.0878	5.0923	0.0022	6.7896	0.0050	4.5292	0.0020	156.59	0.15
hx26run7_014	26	299	5.6317	0.0490	0.11	0.59	5.0668	5.0808	0.0028	6.7613	0.0038	4.5172	0.0020	155.18	0.14
					Avg P GPa	0.0									
hx26run2_003	48	321	5.4994	0.0147	2.27	0.02	5.0564	5.0545	0.0022	6.7193	0.0035	4.4977	0.0019	152.75	0.12
hx26run2_004	78	351	5.4996	0.0192	2.35	0.02	5.0552	5.0573	0.0027	6.7093	0.0053	4.4961	0.0024	152.56	0.17
hx26run2_005	98	371	5.5063	0.0314	2.28	0.04	5.0538	5.0570	0.0036	6.7115	0.0077	4.4932	0.0032	152.50	0.23
hx26run2_007	139	412	5.5119	0.0229	2.29	0.03	5.0530	5.0555	0.0029	6.7120	0.0064	4.4959	0.0026	152.55	0.19
hx26run2_008	160	433	5.5192	0.0184	2.22	0.02	5.0542	5.0547	0.0025	6.7273	0.0040	4.4963	0.0023	152.89	0.14
hx26run2_009	179	452	5.5187	0.0182	2.29	0.02	5.0556	5.0566	0.0023	6.7291	0.0037	4.4973	0.0022	153.03	0.13
hx26run2_010	199	472	5.5245	0.0347	2.24	0.04	5.0572	5.0591	0.0018	6.7333	0.0030	4.4985	0.0015	153.24	0.10
hx26run2_011	216	489	5.5190	0.0120	2.39	0.02	5.0568	5.0602	0.0031	6.7397	0.0049	4.5006	0.0029	153.49	0.18
hx26run2_012	240	513	5.5324	0.0559	2.22	0.07	5.0598	5.0626	0.0037	6.7438	0.0059	4.5030	0.0035	153.74	0.21
hx26run2_014	260	533	5.5313	0.0163	2.30	0.02	5.0596	5.0633	0.0025	6.7439	0.0041	4.5046	0.0024	153.81	0.15
hx26run2_015	280	553	5.5344	0.0196	2.30	0.02	5.0626	5.0659	0.0025	6.7508	0.0041	4.5059	0.0024	154.10	0.15
					Avg P GPa	2.3									
hx26run3_001	25	298	5.4277	0.0467	3.69	0.10	5.0354	5.0450	0.0018	6.7085	0.0032	4.4866	0.0017	151.85	0.11
hx26run3_002	50	323	5.4474	0.0950	3.32	0.17	5.0362	5.0432	0.0015	6.7169	0.0030	4.4860	0.0014	151.96	0.09
hx26run3_004	70	343	5.4360	0.0346	3.63	0.07	5.0366	5.0441	0.0015	6.7121	0.0025	4.4863	0.0014	151.89	0.09
hx26run3_005	91	364	5.4496	0.0674	3.39	0.13	5.0368	5.0428	0.0014	6.7137	0.0024	4.4860	0.0013	151.88	0.08
hx26run3_006	110	383	5.4412	0.0285	3.63	0.06	5.0380	5.0441	0.0016	6.7195	0.0028	4.4859	0.0015	152.04	0.09
hx26run3_007	130	403	5.4504	0.0381	3.49	0.07	5.0388	5.0463	0.0020	6.7199	0.0037	4.4864	0.0019	152.14	0.12
hx26run3_008	150	423	5.4574	0.0692	3.39	0.13	5.0400	5.0462	0.0012	6.7176	0.0022	4.4886	0.0011	152.16	0.07
hx26run3_009	170	443	5.4535	0.0398	3.53	0.08	5.0420	5.0495	0.0014	6.7148	0.0030	4.4889	0.0012	152.20	0.09
hx26run3_010	189	462	5.4617	0.0500	3.42	0.09	5.0440	5.0503	0.0012	6.7247	0.0021	4.4917	0.0011	152.54	0.07
hx26run3_011	210	483	5.4616	0.0500	3.48	0.10	5.0454	5.0505	0.0014	6.7265	0.0026	4.4916	0.0014	152.59	0.09
hx26run3_012	229	502	5.4794	0.0826	3.17	0.14	5.0484	5.0543	0.0021	6.7292	0.0034	4.4956	0.0020	152.90	0.12
hx26run3_013	249	522	5.4804	0.0364	3.21	0.06	5.0510	5.0586	0.0016	6.7414	0.0025	4.4982	0.0015	153.40	0.09
					Avg P GPa	3.5									
hx26run4_001	25	298	5.3718	0.0517	5.05	0.15	5.0200	5.0299	0.0026	6.6959	0.0051	4.4704	0.0024	150.56	0.16
hx26run4_002	51	324	5.3801	0.0275	4.91	0.08	5.0250	5.0334	0.0030	6.7048	0.0048	4.4736	0.0028	150.97	0.17
hx26run4_003	70	343	5.3814	0.0133	4.93	0.04	5.0248	5.0335	0.0023	6.7051	0.0037	4.4743	0.0022	151.01	0.13
hx26run4_004	90	363	5.3845	0.0149	4.91	0.04	5.0264	5.0347	0.0023	6.7094	0.0038	4.4743	0.0022	151.14	0.13
hx26run4_005	110	383	5.3899	0.0133	4.83	0.04	5.0282	5.0367	0.0021	6.7036	0.0046	4.4760	0.0019	151.13	0.14
hx26run4_006	130	403	5.3910	0.0048	4.86	0.01	5.0304	5.0389	0.0021	6.7064	0.0040	4.4786	0.0019	151.34	0.13
hx26run4_007	149	422	5.3968	0.0189	4.77	0.05	5.0330	5.0405	0.0019	6.7145	0.0030	4.4822	0.0018	151.70	0.11
					Avg P GPa	4.9									
hx26run5_007	26	299	5.3889	0.0305	4.62	0.08	5.0201	5.0366	0.0040	6.7135	0.0107	4.4808	0.0034	151.51	0.29
hx26run5_008	48	321	5.3841	0.0174	4.80	0.05	5.0162	5.0293	0.0040	6.7230	0.0110	4.4795	0.0034	151.46	0.30
hx26run5_009	70	343	5.3859	0.0273	4.81	0.07	5.0188	5.0288	0.0029	6.7168	0.0080	4.4789	0.0025	151.29	0.22
hx26run5_010	90	363	5.3897	0.0390	4.78	0.10	5.0210	5.0319	0.0039	6.7142	0.0105	4.4767	0.0032	151.25	0.29
hx26run5_011	111	384	5.3836	0.0167	4.99	0.05	5.0236	5.0300	0.0042	6.7176	0.0104	4.4763	0.0037	151.25	0.29
hx26run5_012	130	403	5.3887	0.0108	4.92	0.03	5.0277	5.0358	0.0040	6.7168	0.0071	4.4791	0.0032	151.50	0.23
hx26run5_013	150	423	5.3896	0.0198	4.95	0.05	5.0296	5.0379	0.0027	6.7172	0.0053	4.4786	0.0024	151.56	0.16
hx26run5_014	170	443	5.3907	0.0299	4.98	0.08	5.0316	5.0408	0.0029	6.7110	0.0056	4.4802	0.0025	151.56	0.18
hx26run5_015	190	463	5.3901	0.0194	5.06	0.05	5.0336	5.0422	0.0023	6.7130	0.0045	4.4811	0.0020	151.68	0.14
hx26run5_016	210	483	5.3949	0.0312	4.99	0.09	5.0366	5.0422	0.0017	6.7230	0.0034	4.4825	0.0015	151.95	0.11
					Avg P GPa	4.9									
hx26run6_001	25	298	5.2411	0.0225	9.08	0.12	5.0067	5.0103	0.0047	6.7114	0.0081	4.4577	0.0036	149.89	0.23
hx26run6_002	25	298	5.2400	0.0166	9.12	0.09	5.0058	5.0168	0.0046	6.7152	0.0078	4.4565	0.0038	150.13	0.26
hx26run6_003	40	313	5.2491	0.0171	8.84	0.09	5.0082	5.0182	0.0036	6.7133	0.0052	4.4571	0.0024	150.15	0.18
hx26run6_004	61	334	5.2554	0.0258	8.68	0.13	5.0120	5.0210	0.0051	6.7188	0.0087	4.4577	0.0040	150.38	0.28
hx26run6_005	81	354	5.2621	0.0377	8.51	0.18	5.0132	5.0230	0.0037	6.7196	0.0063	4.4622	0.0029	150.61	0.21
hx26run6_006	100	373	5.2633	0.0251	8.52	0.12	5.0144	5.0241	0.0035	6.7256	0.0059	4.4614	0.0027	150.75	0.19
hx26run6_007	27	300	5.2382	0.0179	9.19	0.09	5.0080	5.0108	0.0040	6.7120	0.0061	4.4490	0.0028	149.63	0.20
					Avg P GPa	8.8									

850
851
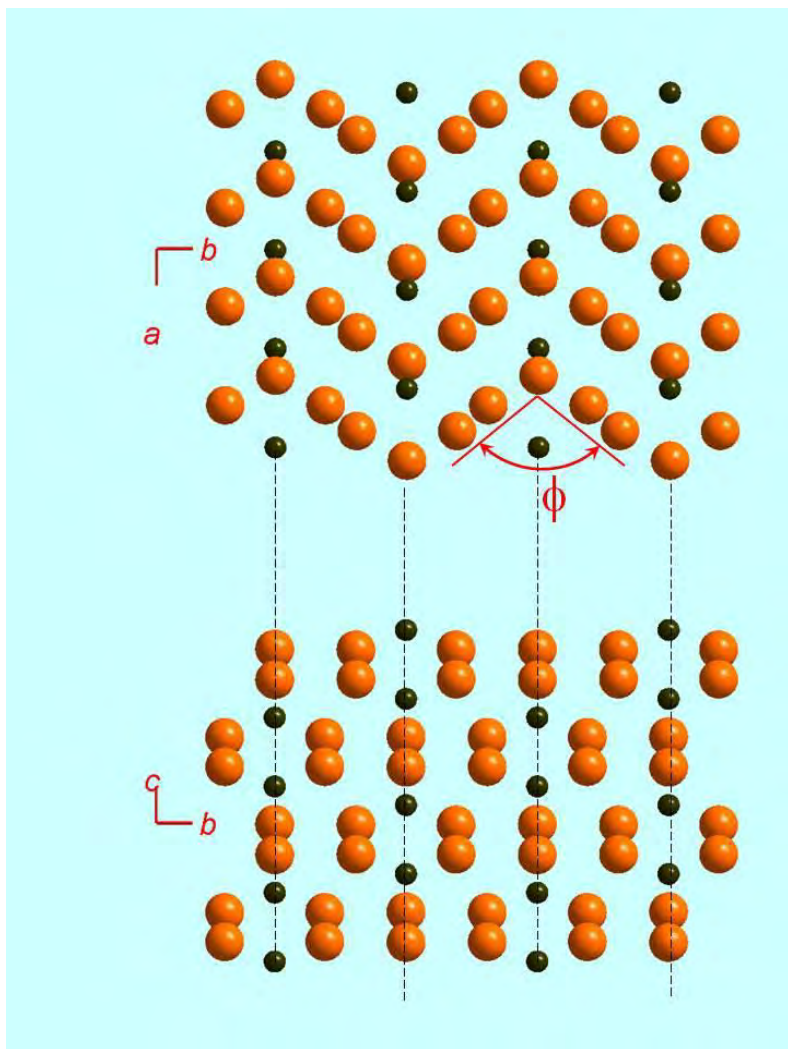
Revision 1 *American Mineralogist* June 2015   42

Table 4 Volumetric coefficients summary				
Compressibility	beta /GPa	Δβ		
Fe-saturated (Dec2012)				
Ferromagnetic	0.0053			
		-0.0019	±0.002/GPa	
Paramagnetic	0.0034			
Thermal expansion	alpha /K	Δα		
Stoichiometric (May 2013)				
Ferromagnetic	4.5E-06			
		6.4E-05	±2E-05/K	
Paramagnetic	6.8E-05			
average Δβ/Δα = dT$_C$/dP =		-30	±20 K/GPa	

852

Fig 1
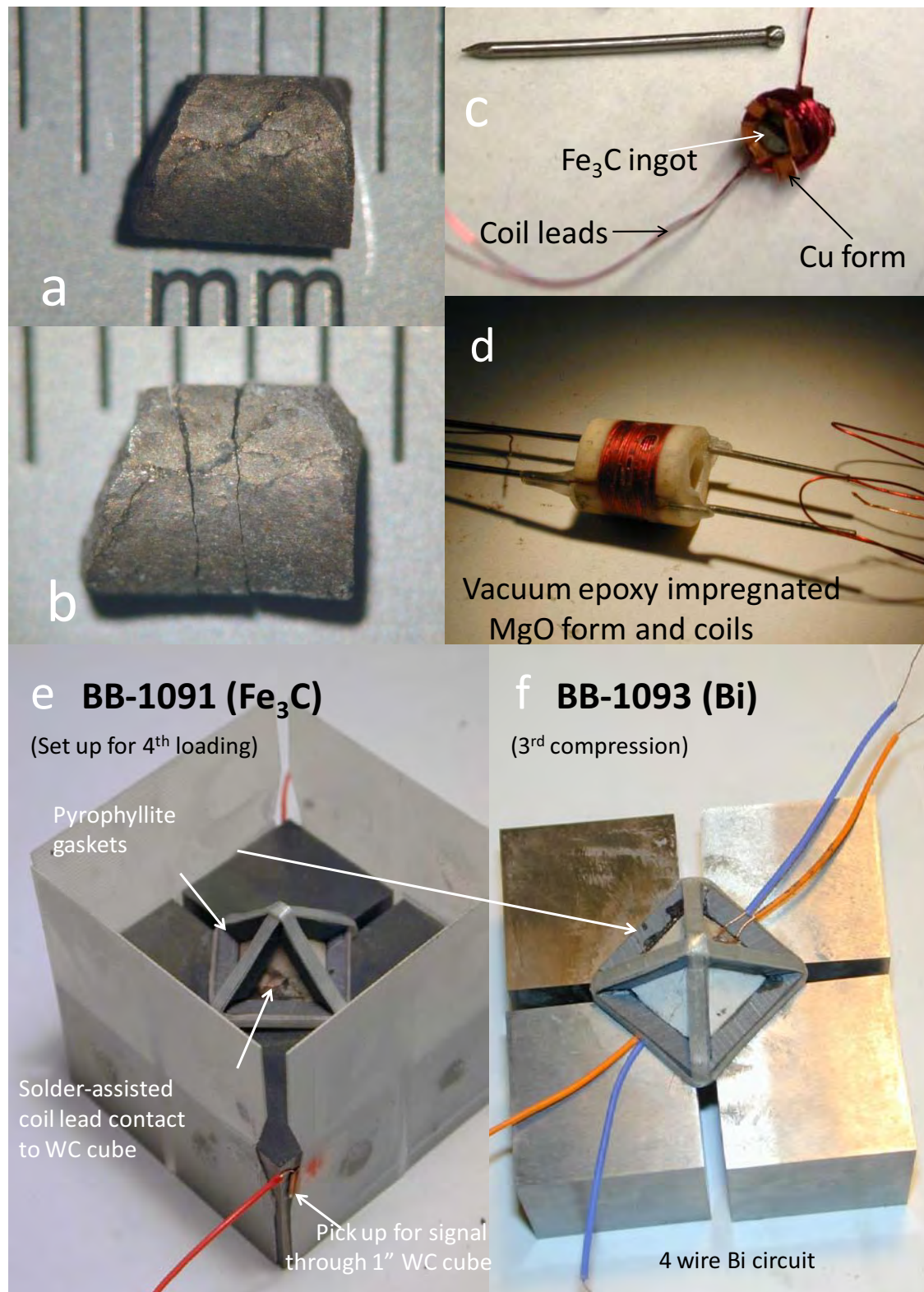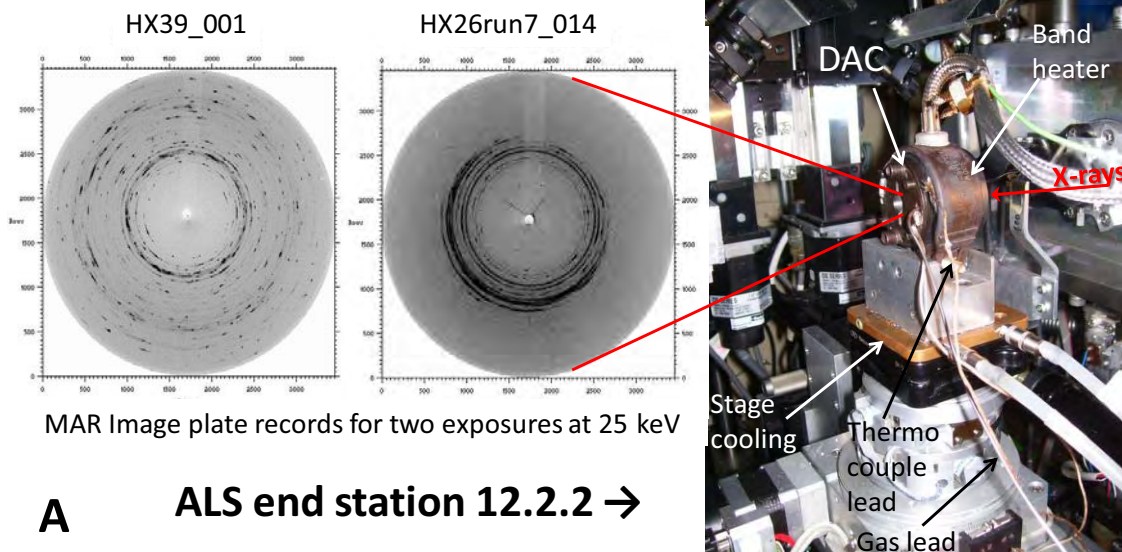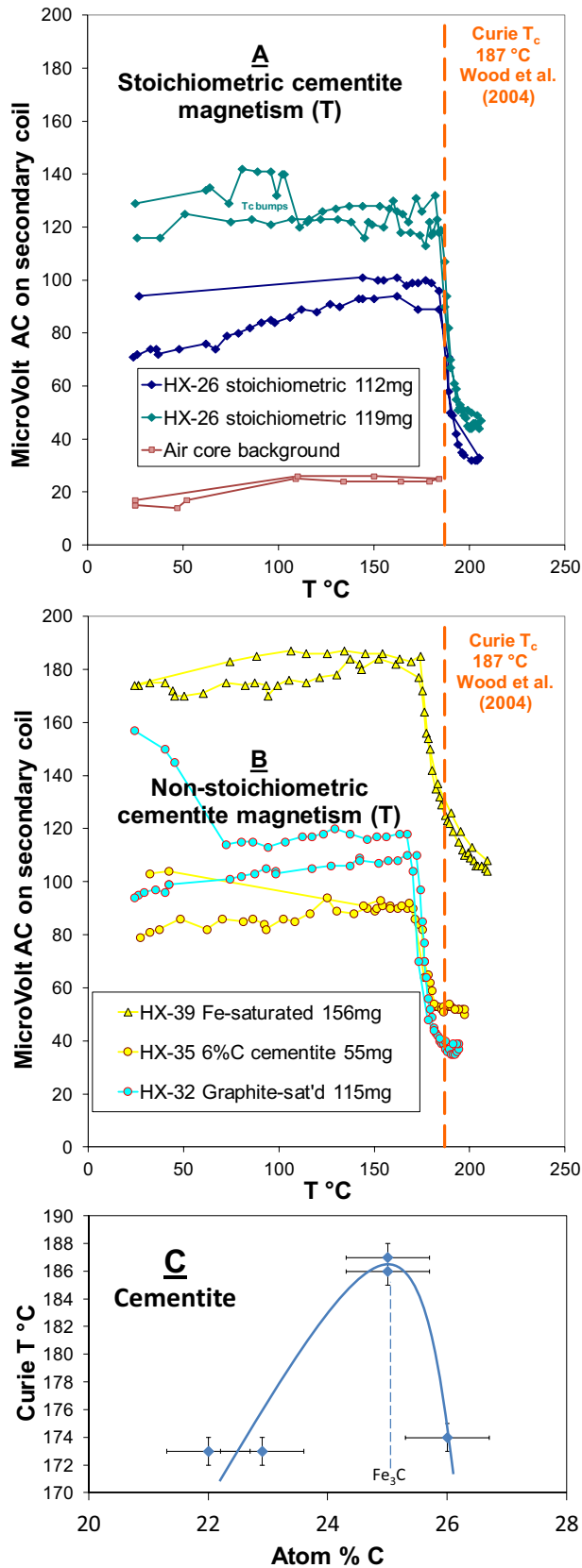
Figure 2

ALS end station 12.2.2 →

A

MAR Image plate records for two exposures at 25 keV

B

Figure 3

4

Figure 4.

5
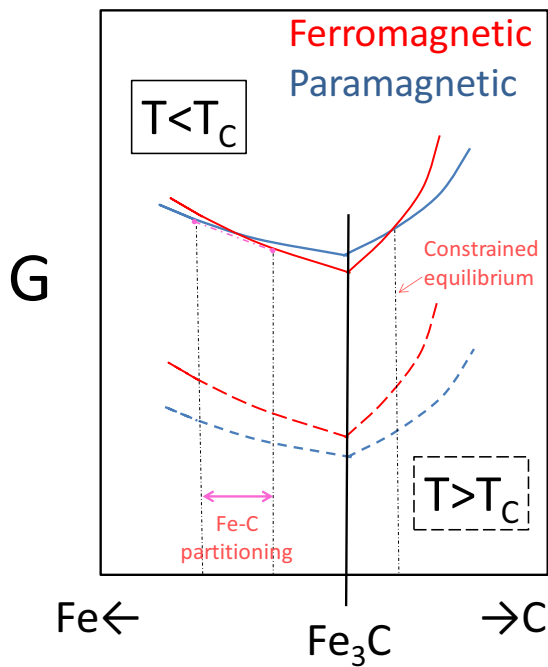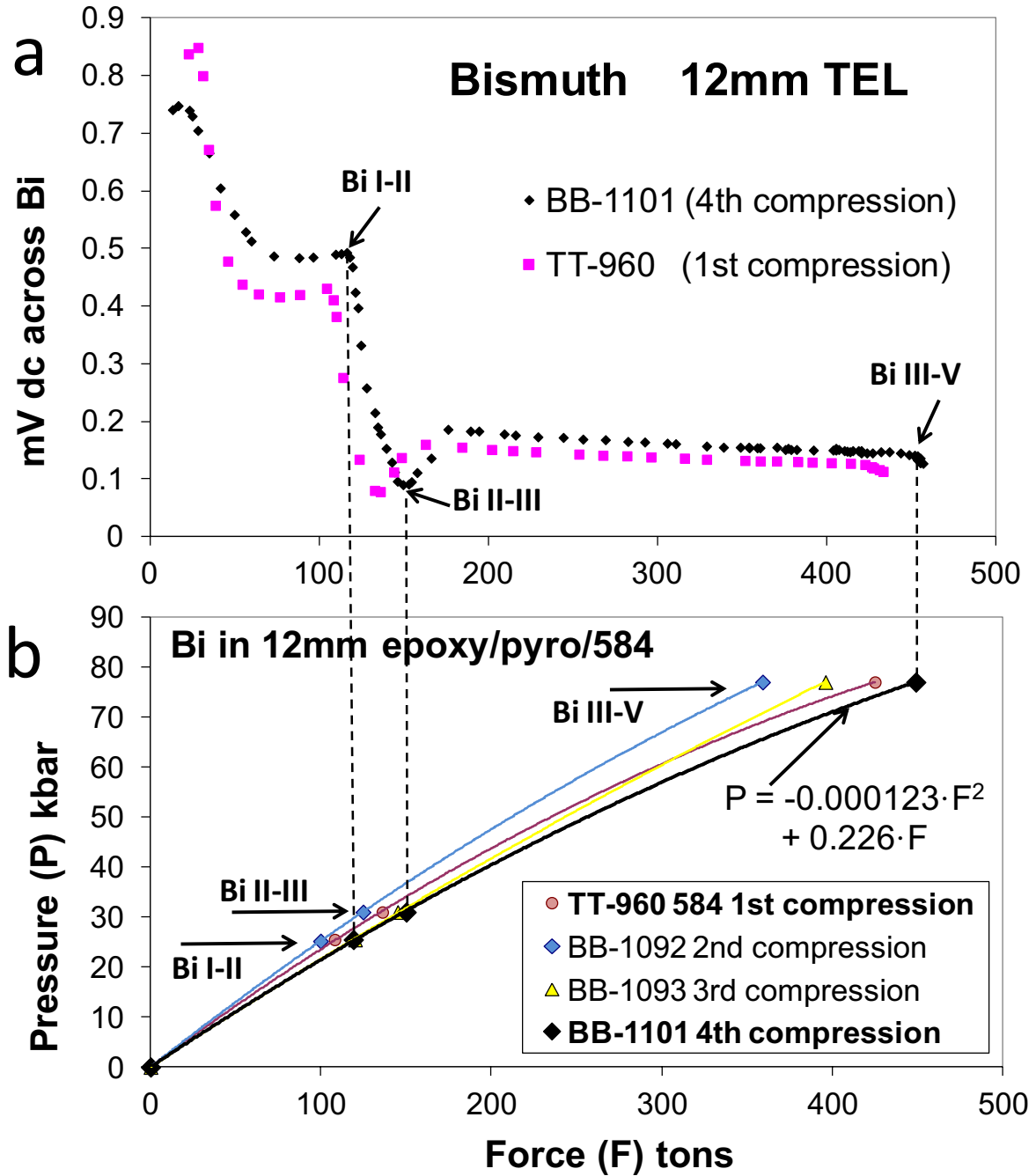
Figure 5

Figure 6

7
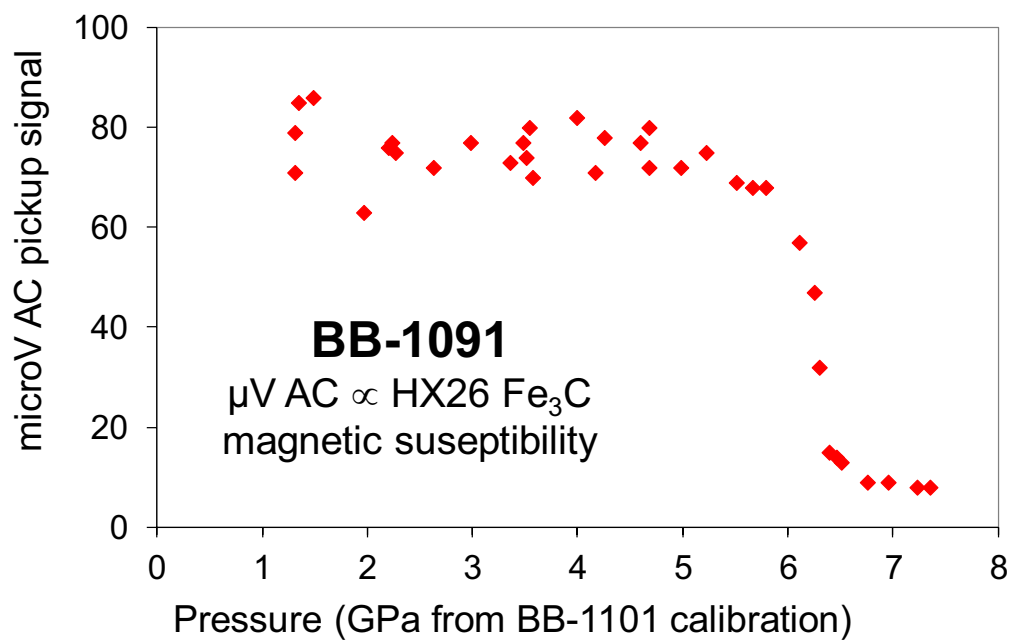
Figure 7

Revision 1 *American Mineralogist* June 2015   8

Figure 8
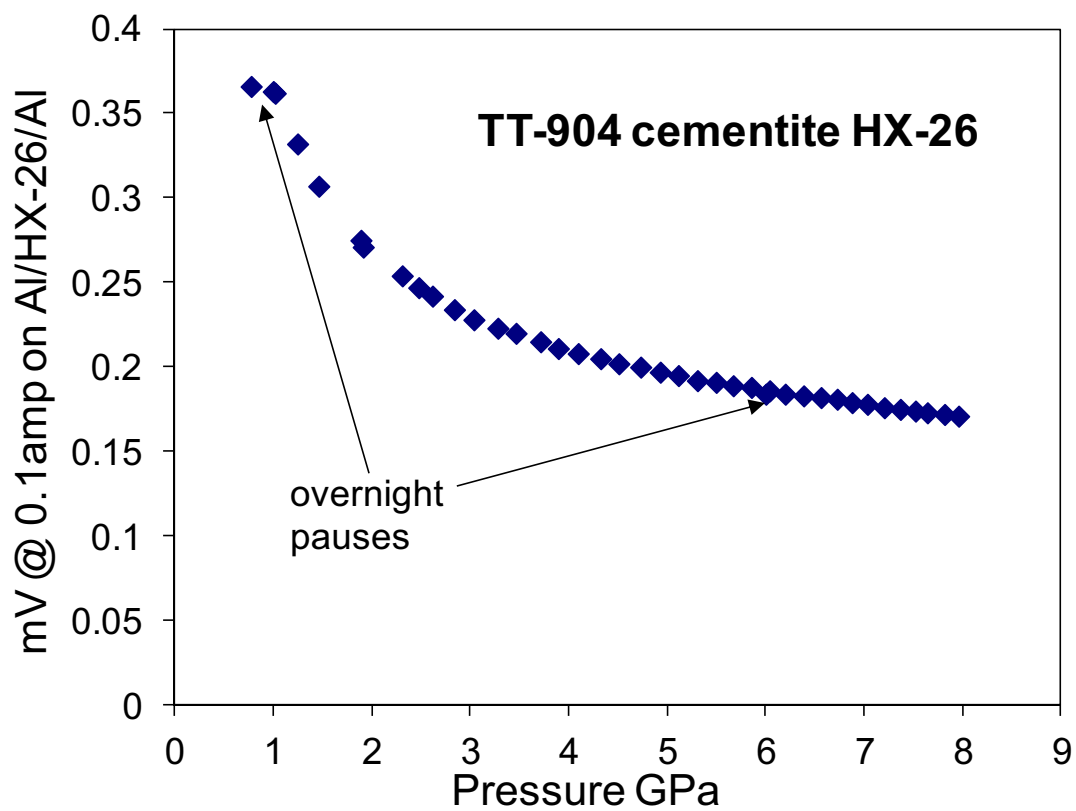
Figure 9

Figure 10

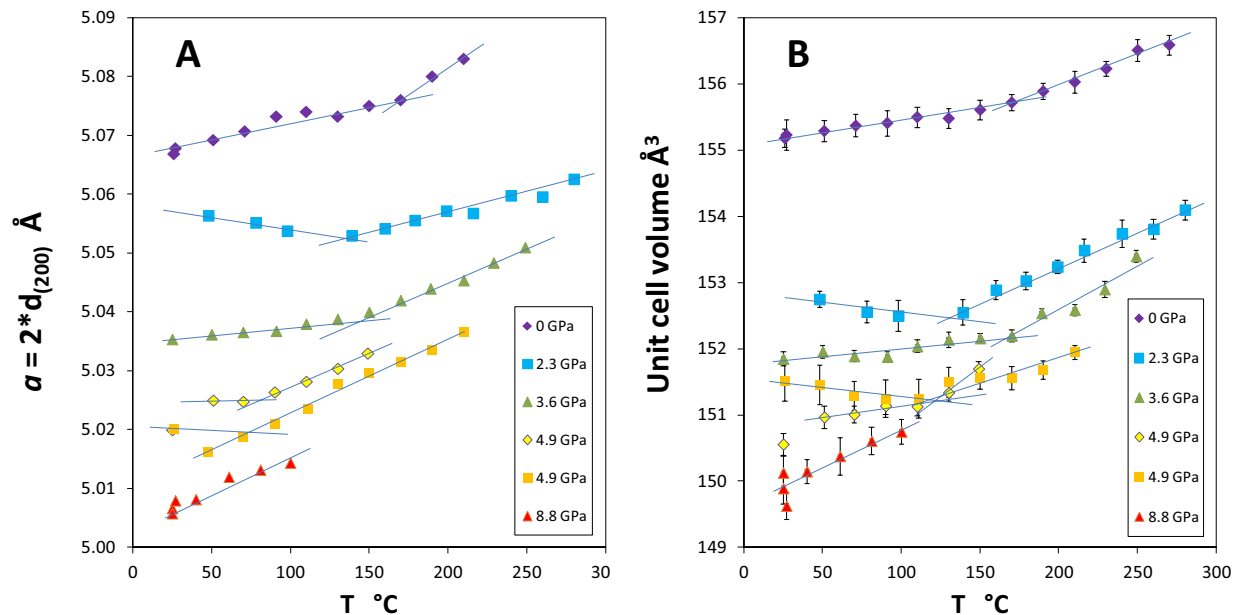**Figure 11**